International Journal of Mechanical Sciences 267 (2024) 109014

Contents lists available at ScienceDirect

International Journal of Mechanical Sciences

journal homepage: www.elsevier.com/locate/ijmecsci

Nonlinear dynamic behavior of carbon nanotubes incorporating size effects

Bo Yang *, Mahmoud Mousavi *

Division of Applied Mechanics, Department of Materials Science and Engineering, Uppsala University, 75103 Uppsala, Sweden

ARTICLE INFO

Keywords:
Carbon nanotubes
Geometrical nonlinear effects
Wave propagation
Size effects
Second strain gradient elasticity

ABSTRACT

This research endeavors to investigate the geometrically nonlinear dynamic characteristics of Carbon Nanotubes (CNTs) while incorporating size effects based on the Second Strain Gradient (SSG) elasticity theory. To this end, the nonlinear governing equations and its corresponding boundary conditions are deduced in alignment with the Green–Lagrange strain tensor and Hamilton's principle. Concurrently, the weak form is expounded through the utilization of the C^3 continuum Hermite interpolation functions, which ensure the continuity and smoothness of higher-order strain and displacement fields. Subsequently, a perturbation methodology is introduced, incorporating nonlinear phenomena into the context of linear wave propagation within the framework of periodic structures theory. The wave propagation characteristics manifest a pronounced disparity between the models based on linear SSG theory and those through nonlinear SSG theory with stiffness hardening phenomenon. In contrast to the zigzag CNTs, armchair CNTs evince an elevated aptitude for wave control. The application of nonlinear SSG theory in combination with the wave finite element method is significant for comprehending the wave propagation characteristics of complex CNTs.

1. Introduction

Nano-electromechanical resonators have seen a burgeoning utilization across a diverse spectrum of nano-scaled apparatus, encompassing nano-sensors, atomic force microscopes, nano-scanning mirrors, and microturbines, as underscored by a multitude of scholarly contributions [1–5]. In this milieu, the Carbon Nanotubes (CNTs), as the waveguides in resonator systems, have garnered substantial interest, owing to their extraordinary attributes such as superior mechanical properties, adeptness in acoustic manipulation, and commendable energy efficiency [6–8]. Consequently, delving into the vibrational and acoustic characteristics of CNTs has emerged as an imperative undertaking. Empirical investigations have discerned that the mechanical properties in nano-scale materials are different from their macro-scale counterparts [9–11]. This delineation posits a formidable challenge to the Classical Theory (CT) of continuum elasticity, which, lacking pertinent length-scale parameters, proves inadequate in encapsulating the distinctive size-dependent attributes. Hence, generalizing the CT is essential to incorporate the size-dependent characteristics of nano-scale materials.

To elucidate the attributes of nano-sized materials, several continuum theories of elasticity have been proposed. These encompass the strain gradient family [12,13], consisting of the Strain Gradient (SG) theory [14,15], the Second Strain Gradient (SSG) theory [16,17], the couple stress theory [18,19], and the modified couple stress theory [20,21]. Additionally, the micro-continuum theory [22,23], inclusive of the micro-polar theory [24], the micro-stretch theory [25], and the micro-morphic theory [26], has been instrumental in this context. Furthermore, the concepts of surface elasticity theory [27,28], as well as the non-local elasticity theory [29,30], have made contributions to the comprehension of nano structures. Significantly, the utilization of the SG theory from the strain gradient family has given rise to a singular predicament at the defect line pertaining to double stresses [31–33]. To surmount this challenge, the SSG theory was introduced, incorporating the potential energy as a function depending on the first, second, and third gradients of displacement. In the domain of couple stress theory, a holistic perspective is adopted by accounting for both conventional deformations and the gradient of the rotation vector in the computation of strain energy. Meanwhile, the modified couple stress theory employs the assumption of symmetry in the couple stress tensor, enforced through the imposition of an equilibrium condition concerning couple stresses. In the micro-polar theory, the emphasis is placed on the independent rotation of the micro-material in the structure, while the micro-stretch theory undertakes the evaluation of the independent stretching scalar within the micro-material. The most comprehensive formulation, known as the micro-morphic theory, accommodates both the rotational and deformative behaviors of the micro-material in the structures. Lastly, the non-local elasticity theory posits that the stress at a given point is related to the strains observed at all points across the

* Corresponding authors.
E-mail addresses: boyang-chn@hotmail.com (B. Yang), mahmoud.mousavi@angstrom.uu.se (M. Mousavi).

https://doi.org/10.1016/j.ijmecsci.2024.109014
Received 4 November 2023; Received in revised form 15 December 2023; Accepted 3 January 2024
Available online 8 January 2024

Nomenclature

CT	Classical Theory
CNTs	Carbon Nanotubes
d_e	Bond length
$\mathcal{E}_s$	Strain energy
$\mathcal{E}_k$	Kinetic energy
$\mathcal{E}_w$	Work done by external loads
$\boldsymbol{\epsilon}$	Symmetrical first displacement gradient
κ	Wave number
$\mathbf{K}^e$	Linear element stiffness matrix
$\mathbf{K}^e_{\mathrm{N}}$	Nonlinear element stiffness matrix
$L_{x,y,z}$	Unit cell length along x, y, z
$l_{a,b,c}$	Higher-order material parameters
$l_{1,2}$	Higher-order inertia parameters
m	Mass of a carbon atom
$\mathbf{M}^e$	Linear element mass matrix
MD	Molecular Dynamics
SG	Strain Gradient
SSG	Second Strain Gradient
SWCNTs	Walled Carbon Nanotubes
WFEM	Wave Finite Element Method
w	Displacement along $\bar{z}$ direction
w'	Rotation in $\bar{x}0\bar{z}$ plane
ω	Frequency
σ	Stress
λ	Wave propagation constant
$\boldsymbol{\xi}$	Second displacement gradient
$\boldsymbol{\zeta}$	Third displacement gradient
η	Damping loss factor
ρ	Mass density
∇	Gradient operator

entirety of the body, thus departing from the classical notion of local stress–strain relationships.

The dynamic characteristics of CNTs have been explored recently in the literature. Notably, Garg et al. [34] undertook a systematic examination aimed at predicting the attributes of Single-Walled Carbon Nanotubes (SWCNTs) by leveraging computational models grounded in diverse methodologies. Ramalingame et al. [35] devised a malleable piezoresistive sensor matrix, founded upon a composite material comprising CNTs, for the measurement of pressure distribution. This innovation demonstrated the utility in dynamic pressure assessment, exemplified by its application in gait analysis within an insole configuration. Furthermore, Esen et al. [36] delved into an investigation of the dynamic responses exhibited by composite beams reinforced with CNTs, employing the nonlocal strain gradient theory as the theoretical framework. The comprehensive analysis encompassed a parameter study, elucidating the ramifications of varying load velocities. Khorshidi [37] employed a modified couple stress theory, featuring a weakening effect, to prognosticate the dispersion characteristics of flexural waves propagating within CNTs. The outcomes evinced a concordance between the predictions derived from the modified couple stress Timoshenko nanobeam model and those ascertained through related Molecular Dynamics (MD) simulations. Izadi et al. [38] engaged in an assessment of non-classical continuum parameters applicable to both armchair and zigzag-configured single-walled CNTs, with an explicit emphasis on size-dependent behaviors during torsional and bending deformations. This endeavor hinged upon the application of micropolar theory, and its findings underscored the inadequacies of the classical Cauchy theory in capturing these effects. Lastly, Dindarloo et al. [39] explored the three-dimensional vibrations of CNTs, utilizing the framework of nonlocal elasticity theory. The consequential results can facilitate future analytical endeavors focused on CNTs.

A substantial body of research has been dedicated to investigating the nonlinear attributes of macro-scale structures, as documented in extant literature sources [40–45]. However, a paucity of investigation exists regarding the nonlinear dynamical phenomena inherent to CNTs. Notably, Vinyas et al. [46] conducted an inquiry into the geometrically nonlinear behavior of Carbon Nanotube-Reinforced Magneto-Electro-Elastic (CNTMEE) doubly curved shells, revealing that both geometric and material parameters exert pronounced influence over the nonlinear characteristics of CNTMEE shells. Likewise, Strozzi et al. [47] delved into the nonlinear resonance interactions and energy exchanges occurring between the bending and circumferential flexure modes in single-walled CNTs. Their numerical model not only substantiates the analytical model's predictions but also demonstrates a good accurate alignment with threshold values for nonlinear energy localization. Additionally, Dat et al. [48] presented an analytical framework for elucidating the nonlinear magneto-electro-elastic vibrations of smart sandwich plates, composed of a nanocomposite featuring Carbon Nanotube Reinforcement (CNTRC). Within this context, numerical simulations elucidate the impacts stemming from variations in geometric parameters, CNTs volume fraction, temperature, and moisture increments. Furthermore, Ghaffari et al. [49] contributed an analytical solution delineating the nonlinear forced vibration response of bridged CNT-based mass sensors subjected to diverse thermal loading conditions and external harmonic excitations. Noteworthy outcomes of their study encompass a comprehensive exploration of the effects of thermal loads and key parameters on nonlinear resonance frequency and amplitude shifts.

Meanwhile, the utilization of periodic nanostructures endowed with distinctive properties has found widespread application across diverse domains of engineering [50–53]. In the pursuit of comprehending the vibrational and acoustic characteristics of these periodic nanostructures, several methodologies have emerged, such as the Wave Finite Element Method (WFEM) [54], as well as the homogenization technique [55–57], which encompasses the asymptotic homogenization method [58,59] and the equivalent strain energy method [60,61]. Among the aforementioned techniques, WFEM stands out as a significant advancement beyond the conventional Finite Element (FE) method, offering the capacity to model intricate structures effectively. Grounded in the principles of periodic structures theory, WFEM streamlines the analysis process by representing a periodic structure as a solitary unit cell, thus mitigating the computational complexity. The investigation of acoustic characteristics in CNTs has garnered considerable scholarly interest. For instance, Gupta et al. [62] scrutinized wave propagation behavior within periodic CNTs while delving into the characterization of buckling phenomena. On the other hand, Asghar et al. [63] undertook an examination of free vibrations in Double-Walled Carbon Nanotubes (DWCNTs) utilizing a non-local elastic shell model. This research has demonstrated the model's proficiency in evaluating the free frequency characteristics of DWCNTs. Furthermore, Al-Furjan et al. [64] delved into the realm of wave propagation analysis within multi-hybrid nanocomposites (MHC) that reinforce doubly curved panels embedded within viscoelastic foundations. By incorporating the viscous parameter, their investigation revealed a transition in the relationship between wavenumber and phase velocity from exponential augmentation to logarithmic amplification.

The extant literature has exhibited a limitation in its attention to the nonlinear wave propagation in periodic CNTs, especially when accounting for size-related effects. This research presents a simulation framework to investigate the geometrically nonlinear dynamic characteristics of CNTs. The approach relies on the application of the SSG theory, known for effectively addressing singularities found in physical field descriptions, most notably the elastic bend–twist tensor,

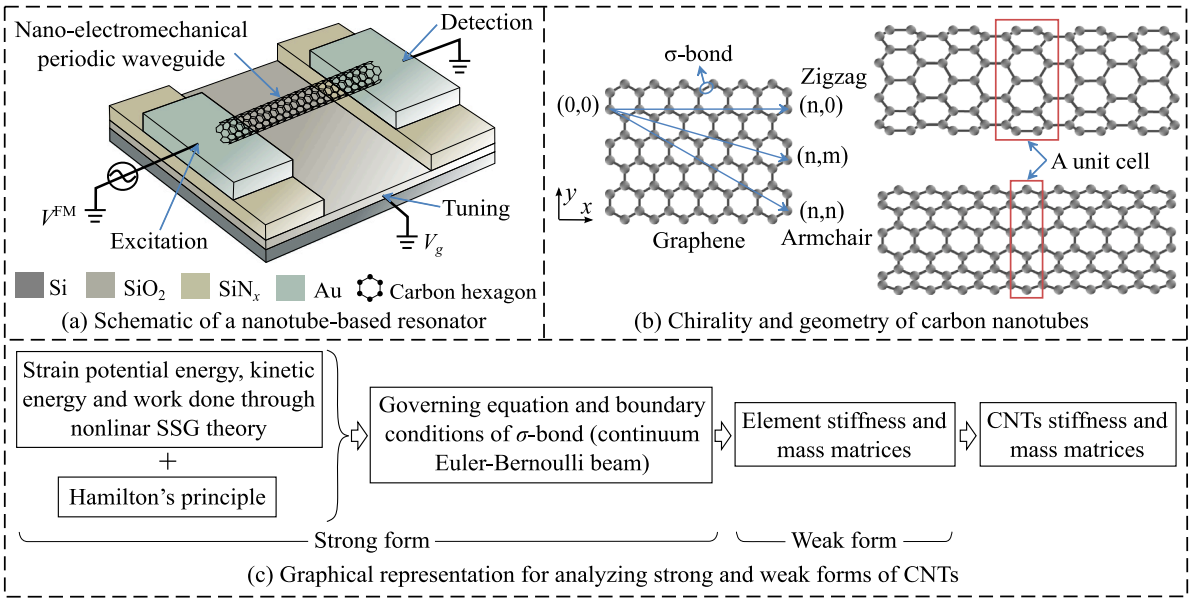

Fig. 1. The schematic of a nano-electromechanical resonator system. (a): The CNTs-based resonator is constructed by excitation port, detection port, tuning, and on chip periodic CNTs-based waveguide. (b): The chirality and geometry of CNTs in the global coordinate system. (c): The graphical representation for analyzing strong and weak forms of CNTs. Based on the nonlinear SSG theory, the governing equation and boundary conditions of a bond can be confirmed. Then the weak form can be deduced from the strong form.

which attains singularity in the SG theory [33,65–67]. Simultaneously, it manifests the size-dependent properties and stiffness hardening phenomena. The proposed numerical framework will be useful for subsequent computational inquiries into the nonlinear dynamic behavior of nanomaterials with size effects. The article is organized as below: Section 2 governs the geometrically nonlinear model of CNTs through the SSG theory. Subsequently, Section 3 delves into the analysis of free nonlinear wave propagation, achieved by the solution of an eigenvalue problem within the framework of WFEM. Section 4 presents an exposition encompassing the dispersion relation, model density, forced response, and displacement field of zigzag and armchair CNTs. Finally, Section 5 concludes the study.

2. Numerical modeling of CNTs

This section commences with the introduction of the geometrically nonlinear model of CNTs. Subsequently, the governing equations, along with its boundary conditions, are derived through the utilization of the SSG theory. Then, the weak formulation is elucidated, wherein the computation of element matrices is performed.

In this study, as delineated in Fig. 1(a), a nano-electromechanical resonator system is introduced, which is predicated upon a waveguide constituted by CNTs and electrical signal ports for the manipulation of its dynamical behavior. The design resides in the modulation of intensity at the electrical excitation port, which is executed at a specific frequency. This modulation engenders a motion within the resonator. The discernment and quantification of this motion are achieved through the monitoring of the reflected signal intensity at the electrical detection port. This strategy allows for the elucidation of the resonator's dynamic response and the characterization of its vibrational modes. As shown in Fig. 1(b), the interactions between carbon atoms are governed by in-plane σ-bonds. The graphical representation for analyzing strong and weak forms of CNTs is presented in Fig. 1(c). In this paper, a fundamental assumption is made that the CNTs are devoid of any defects to warrant a pristine structural integrity. This study is centered upon the continuum mechanics of the zigzag and armchair CNTs. Through the analysis, the complex mechanical properties of CNTs can be revealed, thereby enhancing the understanding of nano-electromechanical systems.

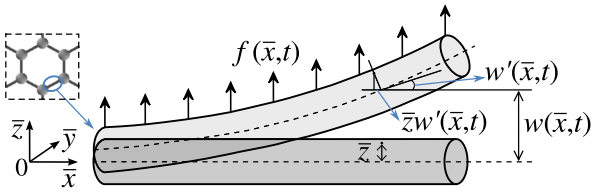

Fig. 2. The σ-bonds are considered as the continuum Euler–Bernoulli beams under lateral distributed loads in the local coordinate system. The displacement vector includes $\bar{z}w'(\bar{x},t)$ along $\bar{x}$ direction and $w(\bar{x},t)$ along $\bar{z}$ direction.

2.1. Derivation of strong form

As shown in Fig. 2, the σ-bond between two carbon atoms is assumed as a continuum Euler–Bernoulli beam with displacement $w(\bar{x},t)$ along $\bar{z}$ direction and rotation $w'(\bar{x},t)$ in $\bar{x}0\bar{z}$ plane. In order to incorporate size effects, the SSG theory as a generalized continuum theory is used. The displacement vector $\mathbf{W}$ at the position $\bar{x}$ can be expressed as:

$$\mathbf{W} = \left(-\bar{z}\frac{\partial w(\bar{x},t)}{\partial \bar{x}},\ 0,\ w(\bar{x},t)\right)^{\top}, \tag{1}$$

where the axial deformation of the beam is ignored under the small deformation condition in this study. In order to investigate the nonlinear properties, the Green–Lagrange strain tensor [68] considering geometrical nonlinearity is utilized, which can be written as:

$$\varepsilon_{11} = -\bar{z}\frac{\partial^2 w(\bar{x},t)}{\partial \bar{x}^2} + \frac{1}{2}\left(\frac{\partial w(\bar{x},t)}{\partial \bar{x}}\right)^2. \tag{2}$$

The expressions of the other non-zero strain tensor components in SSG theory [69] with the first strain gradient $\boldsymbol{\xi}$ and second strain gradient $\boldsymbol{\zeta}$ can be obtained as the follows:

$$\boldsymbol{\xi} = \left(\xi_{111},\ \xi_{113},\ \xi_{131},\ \xi_{311}\right),\ \boldsymbol{\zeta} = \left(\zeta_{1111},\ \zeta_{1113},\ \zeta_{1131},\ \zeta_{1311},\ \zeta_{3111}\right), \tag{3}$$

in which $\xi_{111} = -\bar{z}w''' + w'w''$, $\xi_{113} = -\xi_{131} = -\xi_{311} = w''$, $\zeta_{1111} = -\bar{z}w'''' + \left(w''\right)^2 + w'w'''$, $\zeta_{1113} = -\zeta_{1131} = -\zeta_{1311} = -\zeta_{3111} = w'''$. The superscript $(')$ represents the derivative of $w(\bar{x},t)$ with respect to $\bar{x}$. On the other hand, the strain energy density $\bar{\mathcal{E}}_s$ by the Mindlin's SSG

theory [70] is written as:

$$\overline{\mathcal{E}}_s = \frac{1}{2}\boldsymbol{\varepsilon} : \mathcal{L} : \boldsymbol{\varepsilon} + \frac{1}{2}\boldsymbol{\xi} \ \vdots \ \mathcal{A} \ \vdots \ \boldsymbol{\xi} + \frac{1}{2}\boldsymbol{\zeta} :: \mathcal{B} :: \boldsymbol{\zeta} + \boldsymbol{\varepsilon} : \mathcal{C} :: \boldsymbol{\zeta} + \mathcal{B}_0 :: \boldsymbol{\zeta}, \tag{4}$$

where $\boldsymbol{\varepsilon}$ is the symmetrical first displacement gradient, $\boldsymbol{\xi}$ stands for the second displacement gradient, and $\boldsymbol{\zeta}$ denotes the third displacement gradient. The classical stiffness tensor $\mathcal{L}$ is determined by the conventional *Lamé* parameters λ and μ. Additionally, there are non-classical stiffness tensors $\mathcal{A}$, $\mathcal{B}$, and $\mathcal{C}$ associated with parameters $a_{i(i=1,\ldots,5)}$, $b_{j(j=1,\ldots,7)}$, and $c_{k(k=1,\ldots,3)}$ respectively. $\mathcal{B}_0$ represents the dimension of force related to a cohesion modulus b_0 [70], and ∇ is the gradient operator. In the following, employing the above-mentioned approach on reducing the dimension, the spatial Hamilton's principle will be dimensionally reduced to a beam structure. Substituting Eqs. (2) and (3) into Eq. (4), the strain energy density can be written as:

$$\begin{aligned}\overline{\mathcal{E}}_s =& \frac{1}{2}E\left(\varepsilon_{11}^2 + l_a^2\xi_{111}^2 + l_{a_1}^2\xi_{113}^2 + l_b^4\zeta_{1111}^2 + l_{b_1}^4\zeta_{1113}^2 + 2l_c\varepsilon_{11}\zeta_{1111}\right) \\ &+ b_0\zeta_{1111},\end{aligned} \tag{5}$$

in which l_a, l_{a_1}, l_b, l_{b_1}, and l_c are the higher-order material parameters [16]. Subsequently, the constitutive relations can be obtained as follows:

$$\begin{aligned}&\sigma_{11} = E\left(\varepsilon_{11} + l_c\zeta_{1111}\right),\ \sigma_{111} = El_a^2\xi_{111},\ \sigma_{113} = El_{a_1}^2\xi_{113}, \\ &\sigma_{1111} = E\left(l_b^4\zeta_{1111} + l_c\varepsilon_{11}\right) + b_0,\ \sigma_{1113} = El_{b_1}^4\zeta_{1113}.\end{aligned} \tag{6}$$

Then, the total strain energy can be derived by integrating $\overline{\mathcal{E}}_s$ over its volume, one arrives:

$$\begin{aligned}\mathcal{E}_s =& \int_0^{d_L}\int_A \overline{\mathcal{E}}_s \mathrm{d}A\mathrm{d}\overline{x} = \frac{1}{2}EI\left[G + \left(l_a^2 + l_{b_1}^4\frac{A}{I}\right)G_a + l_b^4 G_b + l_c G_c\right] \\ &+ b_0 A G_0,\end{aligned} \tag{7}$$

in which A is the cross-sectional area and d denotes the length of an element. The definitions of G, G_a, G_b, G_c, and G_0 are given in Appendix A. On the other hand, the kinetic energy, including its classical and non-classical constituents, can be expressed in the following form:

$$\begin{aligned}\mathcal{E}_k =& \frac{1}{2}\rho\int_0^{d_L}\int_A\left[\left(\frac{\partial\mathbf{W}}{\partial t}\right)^2 + l_1^2\left(\frac{\partial^2\mathbf{W}}{\partial\overline{x}\partial t}\right)^2 + l_2^4\left(\frac{\partial^3\mathbf{W}}{\partial\overline{x}^2\partial t}\right)^2\right]\mathrm{d}A\mathrm{d}\overline{x} \\ =& \frac{1}{2}\rho\int_0^{d_L}\left[A\left(\frac{\partial w(\overline{x},t)}{\partial t}\right)^2 + \left(I + l_1^2 A\right)\left(\frac{\partial^2 w(\overline{x},t)}{\partial\overline{x}\partial t}\right)^2\right. \\ &+ \left(l_1^2 I + l_2^4 A\right)\left(\frac{\partial^3 w(\overline{x},t)}{\partial\overline{x}^2\partial t}\right)^2 \\ &\left.+ l_2^4 I\left(\frac{\partial^4 w(\overline{x},t)}{\partial\overline{x}^3\partial t}\right)^2\right]\mathrm{d}\overline{x},\end{aligned} \tag{8}$$

where l_1 and l_2 are the higher-order inertia parameters [16]. $I = \int_A \overline{z}^2\mathrm{d}A$ is the cross-sectional moment of inertia about $\overline{y}$-axis. Furthermore, the work done by external loads can be ascertained as follows:

$$\begin{aligned}\mathcal{E}_w =& \int_0^{d_L} f(\overline{x},t)w(\overline{x},t)\mathrm{d}\overline{x} + f_0 w(\overline{x},t)\Big|_0^{d_L} + f_1\frac{\partial w(\overline{x},t)}{\partial\overline{x}}\Big|_0^{d_L} \\ &+ f_2\frac{\partial^2 w(\overline{x},t)}{\partial\overline{x}^2}\Big|_0^{d_L} + f_3\frac{\partial^3 w(\overline{x},t)}{\partial\overline{x}^3}\Big|_0^{d_L},\end{aligned} \tag{9}$$

in which $f(\overline{x},t)$ indicates the classical distributed load, f_0 denotes the classical nodal load, f_1 is the classical nodal bending moment, and $f_{2,3}$ represent the higher-order end-sectional loads.

In this step, the utilization of the Hamilton's principle [69] is invoked within the framework of the SSG theory to elucidate the strong form, as delineated hereafter:

$$\int_{t_1}^{t_2}(\delta\mathcal{E}_k - \delta\mathcal{E}_s + \delta\mathcal{E}_w)\mathrm{d}t = 0, \tag{10}$$

where $\delta\mathcal{E}_k$, $\delta\mathcal{E}_s$, and $\delta\mathcal{E}_w$ represent the variations of kinetic energy, strain energy, and work of external forces, respectively. Then, from Eqs. (7), (8), (9), and (10), the governing equations are obtained as:

$$\begin{aligned}&EI\left[\left(1 + \frac{A}{I}l_{a_1}^2\right)H_1 + \left(2l_c - l_a^2 - \frac{A}{I}l_{b_1}^4\right)H_2 + l_b^4 H_3\right] \\ &- EA\left[H_4 + \left(2l_c - l_a^2\right)H_5 + l_b^4 H_6\right] \\ &- \rho I H_7 + \rho A H_8 - f(\overline{x},t) = 0,\end{aligned} \tag{11}$$

with associated boundary conditions presented in Appendix B. The detailed expressions of H_1, H_2, H_3, H_4, H_5, H_6, H_7, and H_8 are given in Appendix C. In order to confirm the analytical solution of nonlinear beam addressed in Eq. (11), the displacement and force are considered to be harmonic with amplitudes w_a and f_a, respectively: $w = w_a\cos(\omega t - \kappa\overline{x})$, $f = f_a\cos(\omega t - \kappa\overline{x})$. Here, to solve the nonlinear problem, $\cos^3(\omega t - \kappa\overline{x})$ is linearized as $\frac{3}{4}\cos(\omega t - \kappa\overline{x})$. Then, the governing equations for the analytical solution will be:

$$K_a w_a - K_{a_N} w_a^3 - M_a\omega^2 w_a = f_a, \tag{12}$$

with

$$\begin{aligned}K_a &= EI\left[\left(1 + \frac{A}{I}l_{a_1}^2\right)\kappa^4 - \left(2l_c - l_a^2 - \frac{A}{I}l_{b_1}^4\right)\kappa^6 + l_b^4\kappa^8\right], \\ K_{a_N} &= EA\left[\frac{9}{8}\kappa^4 - \frac{9}{2}\left(2l_c - l_a^2\right)\kappa^6 + 18l_b^4\kappa^8\right], \\ M_a &= \rho I\left[\left(1 + \frac{A}{I}l_1^2\right)\kappa^2 + \left(l_1^2 + \frac{A}{I}l_2^4\right)\kappa^4 + l_2^4\kappa^6\right] + \rho A,\end{aligned} \tag{13}$$

in which K_a is the linear stiffness, K_{a_N} denotes the nonlinear stiffness, M_a is the mass, κ represents the wavenumber, and ω denotes the frequency.

2.2. Finite element calculations

This step entails transforming the strong form into its respective weak form. According to the SSG theory, there exist four Degrees of Freedom (DOFs), w_i, w_i', w_i'', and $w_i'''(i = 1,2)$, on each node of a 1D element with length d_e, which can be written as:

$$\begin{aligned}\mathbf{w}^e(t) =& \left(w|_{\overline{x}=0},\ \frac{\partial w}{\partial\overline{x}}\Big|_{\overline{x}=0},\ \frac{\partial^2 w}{\partial\overline{x}^2}\Big|_{\overline{x}=0},\ \frac{\partial^3 w}{\partial\overline{x}^3}\Big|_{\overline{x}=0},\ w|_{\overline{x}=d_e},\ \frac{\partial w}{\partial\overline{x}}\Big|_{\overline{x}=d_e},\right. \\ &\left.\frac{\partial^2 w}{\partial\overline{x}^2}\Big|_{\overline{x}=d_e},\ \frac{\partial^3 w}{\partial\overline{x}^3}\Big|_{\overline{x}=d_e}\right)^{\top}.\end{aligned} \tag{14}$$

To ensure the continuity of high-order displacement, an eight-term polynomial function is employed for the purpose of interpolating the scalar field denoted as w within a 1D elemental domain:

$$w = \left(1, \overline{x}, \overline{x}^2, \overline{x}^3, \overline{x}^4, \overline{x}^5, \overline{x}^6, \overline{x}^7\right)\left(r_0, r_1, r_2, r_3, r_4, r_5, r_6, r_7\right)^{\top} = \mathbf{xr}. \tag{15}$$

By replacing w into Eq. (14), a reformulation of the nodal displacement vector $\mathbf{w}^e(t)$ can be re-expressed as:

$$\mathbf{w}^e = \begin{bmatrix} 1 & 0 & 0 & 0 & 0 & 0 & 0 & 0 \\ 0 & 1 & 0 & 0 & 0 & 0 & 0 & 0 \\ 0 & 0 & 2 & 0 & 0 & 0 & 0 & 0 \\ 0 & 0 & 0 & 6 & 0 & 0 & 0 & 0 \\ 1 & d_e & d_e^2 & d_e^3 & d_e^4 & d_e^5 & d_e^6 & d_e^7 \\ 0 & 1 & 2d_e & 3d_e^2 & 4d_e^3 & 5d_e^4 & 6d_e^5 & 7d_e^6 \\ 0 & 0 & 2 & 6d_e & 12d_e^2 & 20d_e^3 & 30d_e^4 & 42d_e^5 \\ 0 & 0 & 0 & 6 & 24d_e & 60d_e^2 & 120d_e^3 & 210d_e^4 \end{bmatrix}\begin{bmatrix} r_0 \\ r_1 \\ r_2 \\ r_3 \\ r_4 \\ r_5 \\ r_6 \\ r_7 \end{bmatrix} = \mathbf{dr}. \tag{16}$$

Then, combining Eq. (15) with Eq. (16), the displacement field can be confirmed through the utilization of the C^3 continuum Hermite interpolation function in conjunction with the nodal displacement vector:

$$w = \mathbf{x}\mathbf{d}^{-1}\mathbf{w}^e = \begin{bmatrix} 1-(35\overline{x}^4)/d_e^4+(84\overline{x}^5)/d_e^5-(70\overline{x}^6)/d_e^6+(20\overline{x}^7)/d_e^7 \\ \overline{x}-(20\overline{x}^4)/d_e^3+(45\overline{x}^5)/d_e^4-(36\overline{x}^6)/d_e^5+(10\overline{x}^7)/d_e^6 \\ \overline{x}^2/2-(5\overline{x}^4)/d_e^2+(10\overline{x}^5)/d_e^3-(15\overline{x}^6)/(2d_e^4)+(2\overline{x}^7)/d_e^5 \\ \overline{x}^3/6-(2\overline{x}^4)/(3d_e)+\overline{x}^5/d_e^2-(2\overline{x}^6)/(3d_e^3)+\overline{x}^7/(6d_e^4) \\ (35\overline{x}^4)/d_e^4-(84\overline{x}^5)/d_e^5+(70\overline{x}^6)/d_e^6-(20\overline{x}^7)/d_e^7 \\ -(15\overline{x}^4)/d_e^3+(39\overline{x}^5)/d_e^4-(34\overline{x}^6)/d_e^5+(10\overline{x}^7)/d_e^6 \\ (5\overline{x}^4)/(2d_e^2)-(7\overline{x}^5)/d_e^3+(13\overline{x}^6)/(2d_e^4)-(2\overline{x}^7)/d_e^5 \\ -\overline{x}^4/(6d)+\overline{x}^5/(2d_e^2)-\overline{x}^6/(2d_e^3)+\overline{x}^7/(6d_e^4) \end{bmatrix}\mathbf{w}^e = \mathbf{P}\mathbf{w}^e, \tag{17}$$

in which $\mathbf{P}$ is the interpolating function. In this part, aimed at ascertaining the weak formulation, the first step entails the application of the test function w_t to the governing equations. Subsequently, an integration by parts operation is conducted with respect to the variable $\overline{x}$. Following this, through the employment of Eq. (17), in conjunction with $w_t = \mathbf{P}\mathbf{w}_t^e$, the matrix representation of the geometrically nonlinear governing equations for an element is unequivocally established:

$$\begin{aligned} &EI\int_0^{d_e}\left[\left(1+\frac{A}{I}l_{a_1}^2\right)\mathbf{P}''^{\top}\mathbf{P}''-\left(2l_c-l_a^2-\frac{A}{I}l_{b_1}^4\right)\mathbf{P}'''^{\top}\mathbf{P}'''\right. \\ &\left.+l_b^4\mathbf{P}''''^{\top}\mathbf{P}''''\right]\mathrm{d}\overline{x}\mathbf{w}^e \\ &+EA\int_0^{d_e}\left[\frac{1}{2}\mathbf{P}'^{\top}(\mathbf{P}'^2\mathbf{P}')-\left(2l_c-l_a^2\right)\left(\mathbf{P}''^{\top}(\mathbf{P}'^2\mathbf{P}'')+\mathbf{P}'^{\top}(\mathbf{P}''^2\mathbf{P}')\right)\right. \\ &+l_b^4\left(\mathbf{P}'''^{\top}(\mathbf{P}'^2\mathbf{P}''')\right. \\ &\left.\left.+\frac{2}{3}\mathbf{P}''^{\top}(\mathbf{P}''^2\mathbf{P}'')+\mathbf{P}'^{\top}(\mathbf{P}'''^2\mathbf{P}')\right)\right]\mathrm{d}\overline{x}\mathbf{w}^{e3} \\ &+\rho\int_0^{d_e}\left[A\mathbf{P}^{\top}\mathbf{P}+\left(I+Al_1^2\right)\mathbf{P}'^{\top}\mathbf{P}'+Il_2^4\mathbf{P}'''^{\top}\mathbf{P}'''\right. \\ &\left.+\left(Il_1^2+Al_2^4\right)\mathbf{P}''^{\top}\mathbf{P}''\right]\mathrm{d}\overline{x}\ddot{\mathbf{w}}^e-\int_0^{d_e}\mathbf{P}^{\top}f\mathrm{d}\overline{x}+\mathbf{P}^{\top}f_0\Big|_0^{d_e}+\mathbf{P}'^{\top}f_1\Big|_0^{d_e} \\ &+\mathbf{P}''^{\top}f_2\Big|_0^{d_e}+\mathbf{P}'''^{\top}f_3\Big|_0^{d_e} \\ =&\mathbf{K}^e\mathbf{w}^e+\mathbf{K}_{\mathrm{N}}^e\mathbf{w}^{e3}+\mathbf{M}^e\ddot{\mathbf{w}}^e-\mathbf{F}^e=0, \end{aligned} \tag{18}$$

in which the matrices $\mathbf{K}^e$ and $\mathbf{M}^e$ indicate the linear stiffness and mass matrices, respectively, and $\mathbf{K}_{\mathrm{N}}^e$ is the nonlinear stiffness matrices, while $\mathbf{F}^e$ represents the linear force vector. The superscript $(')$ designates the partial derivative with respect to the coordinate $\overline{x}$. Here, the Young's modulus E of the nanotube's σ-bond can be confirmed as [71,72]:

$$E=\frac{k_t^2 d_e}{4\pi k_b}, \tag{19}$$

where $k_t = 6.52\times10^{-7}$ (N nm^{-1}) is the σ-bond tension stiffness, $k_b = 8.76\times10^{-10}$ (N nm rad^{-2}) indicates the σ-bond bending stiffness.

3. Nonlinear wave motion in periodic structures

Following the results of characterizing nonlinear elements matrices in the previous part, this section starts with the deduction of the dynamic equilibrium equation of a unit cell. Subsequently, the components pertaining to frequency and displacement within the perturbed system are delineated. Thereafter, an investigation into the 1D wave motion characteristics is conducted by means of solving the eigenvalue problem within the framework of periodic structures theory.

The dynamic equilibrium formulations of a unit cell can be written as:

$$\mathbf{K}\left(\mathbf{w}+\frac{\eta}{\omega}\dot{\mathbf{w}}\right)+\mathbf{M}\ddot{\mathbf{w}}=\mathbf{F}-\mathbf{K}_{\mathrm{N}}\mathbf{w}^3, \tag{20}$$

where $\mathbf{K}$, $\mathbf{K}_{\mathrm{N}}$, and $\mathbf{M}$ are the stiffness and mass matrices of a unit cell assembled by $\mathbf{K}^e$, $\mathbf{K}_{\mathrm{N}}^e$, and $\mathbf{M}^e$, respectively. $\mathbf{u}$ denotes the nodal displacement vector. $\mathbf{F}$ represents nodal force vector. η indicates the damping loss factor caused by internal friction within the material.

A scheme for the 1D periodic structure and its unit cell is given in Fig. 3. The harmonic displacement ($\mathbf{w}$) and force ($\mathbf{F}$) components [54] as shown in Fig. 3(b) can be formulated as follows:

$$\mathbf{w}=\hat{\mathbf{w}}e^{\mathrm{i}\omega t},\ \mathbf{F}=\hat{\mathbf{F}}e^{\mathrm{i}\omega t}, \tag{21}$$

in which $\hat{\mathbf{w}}=\mathrm{X}_{\mathrm{w}}\boldsymbol{\Psi}_{\mathrm{w}}$ and $\hat{\mathbf{F}}=\mathrm{X}_{\mathrm{F}}\boldsymbol{\Psi}_{\mathrm{F}}$, with the amplitude vector $\mathbf{X}$ and the eigenvector $\boldsymbol{\Psi}$. ω is the frequency and t indicates the time. Here, the expression $e^{\mathrm{i}\omega t}$ is equivalently replaced by $\cos(\omega t)$. The expression $\cos^3(\omega t)$ is subjected to a linearization process, resulting in the transformed expression $\frac{3}{4}\cos(\omega t)$. Subsequently, the dynamic equilibrium formulations of a unit cell can be re-written as:

$$\left[(1+\mathrm{i}\eta)\mathbf{K}-\omega^2\mathbf{M}\right]\hat{\mathbf{w}}=\hat{\mathbf{F}}-\frac{3}{4}\mathbf{K}_{\mathrm{N}}\hat{\mathbf{w}}^3. \tag{22}$$

In order to delineate the perturbed response of the structural system, an inherent perturbation parameter denoted as α is introduced into the analytical framework. By employing the Linstedt–Poincaré methodology [73], Eq. (22) can be subjected to an asymptotic expansion. Notably, the nonlinear stiffness matrix ($\mathbf{K}_{\mathrm{N}}$) can be represented as $\alpha\boldsymbol{\mathcal{K}}_{\mathrm{N}}$, with the perturbation parameter α serving as a quantifier for the degree of nonlinearity inherent in the system. Concurrently, the frequency and displacement components characterizing the perturbed system can be elucidated via the first-order Linstedt–Poincaré expansion [73], which is written as:

$$\mathbf{w}=\mathbf{w}_0+\alpha\mathbf{w}_1+\cdots+\circ(\alpha^n\mathbf{w}_n),\ \omega=\omega_0+\alpha\omega_1+\cdots+\circ(\alpha^n\omega_n). \tag{23}$$

Upon substituting Eq. (23) into Eq. (22), the linear contribution denoted as $\circ(\alpha^0)$ and the first-order contribution designated as $\circ(\alpha^1)$ can be confirmed, one arrives at:

$$\begin{aligned} &\circ(\alpha^0):\ \left[(1+\mathrm{i}\eta)\mathbf{K}-\omega_0^2\mathbf{M}\right]\hat{\mathbf{w}}_0=\hat{\mathbf{F}}, \\ &\circ(\alpha^1):\ \left[(1+\mathrm{i}\eta)\mathbf{K}-\omega_0^2\mathbf{M}\right]\hat{\mathbf{w}}_1=2\omega_0\omega_1\mathbf{M}\hat{\mathbf{w}}_0-\frac{3}{4}\boldsymbol{\mathcal{K}}_{\mathrm{N}}\hat{\mathbf{w}}_0^3. \end{aligned} \tag{24}$$

It is imperative to emphasize that the internal DOFs remain impervious to the influence of external forces, as the coupling effects are strictly localized within the confines of the unit cell's boundaries. Consequently, it follows that $\mathbf{F}^{\mathrm{I}}=0$, and $\circ(\alpha^0)$ part in Eq. (24) can be written as follows:

$$\left\{(1+\mathrm{i}\eta)\begin{bmatrix}\mathbf{K}^{\mathrm{LL}} & \mathbf{K}^{\mathrm{LR}} & \mathbf{K}^{\mathrm{LI}}\\ \mathbf{K}^{\mathrm{RL}} & \mathbf{K}^{\mathrm{RR}} & \mathbf{K}^{\mathrm{RI}}\\ \mathbf{K}^{\mathrm{IL}} & \mathbf{K}^{\mathrm{IR}} & \mathbf{K}^{\mathrm{II}}\end{bmatrix}-\omega_0^2\begin{bmatrix}\mathbf{M}^{\mathrm{LL}} & \mathbf{M}^{\mathrm{LR}} & \mathbf{M}^{\mathrm{LI}}\\ \mathbf{M}^{\mathrm{RL}} & \mathbf{M}^{\mathrm{RR}} & \mathbf{M}^{\mathrm{RI}}\\ \mathbf{M}^{\mathrm{IL}} & \mathbf{M}^{\mathrm{IR}} & \mathbf{M}^{\mathrm{II}}\end{bmatrix}\right\}\begin{pmatrix}\hat{\mathbf{w}}_0^{\mathrm{L}}\\ \hat{\mathbf{w}}_0^{\mathrm{R}}\\ \hat{\mathbf{w}}_0^{\mathrm{I}}\end{pmatrix} =\begin{pmatrix}\hat{\mathbf{F}}^{\mathrm{L}}\\ \hat{\mathbf{F}}^{\mathrm{R}}\\ \mathbf{0}\end{pmatrix}, \tag{25}$$

where the superscript L denotes the left-side boundary of the unit cell, while R indicates the right-side boundary of the unit cell, as illustrated in Fig. 3(b). The displacement vector in consonance with the theoretical framework of periodic structures involves the deployment of the wavenumber denoted as κ:

$$\hat{\mathbf{w}}_0^{\mathrm{R}}=e^{-\mathrm{i}\kappa L_x}\hat{\mathbf{w}}_0^{\mathrm{L}}. \tag{26}$$

At the same time, when considering the free propagation of waves, one can deduce that the sum of nodal forces exerted on all elements connected to nodes is zero:

$$e^{-\mathrm{i}\kappa L_x}\hat{\mathbf{F}}^{\mathrm{L}}+\hat{\mathbf{F}}^{\mathrm{R}}=0. \tag{27}$$

Eqs. (26) and (27) list the periodic boundary conditions for the unit cell. As a result, the determination of frequency ω can be confirmed through combining the solutions pertaining to the linear zero-order system and the perturbed system, this yields:

$$\omega(\kappa)=\omega_0(\kappa)+\omega^*(\kappa), \tag{28}$$

with $\omega^*(\kappa)=\alpha\omega_1=\left[3\mathrm{X}_0^{\mathrm{b}2}\boldsymbol{\Psi}_0^{\mathrm{b}\top}\mathbf{T}_1\mathbf{K}_{\mathrm{N}}\left(\mathbf{T}_2\boldsymbol{\Psi}_0^{\mathrm{b}}\right)^3\right]\Big/\left[8\omega_0\boldsymbol{\Psi}_0^{\mathrm{b}\top}\mathbf{T}_1\mathbf{M}\mathbf{T}_2\boldsymbol{\Psi}_0^{\mathrm{b}}\right]$.

The detailed derivation process of perturbed system is given in Appendix D. On the other hand, modal density is one statistics based

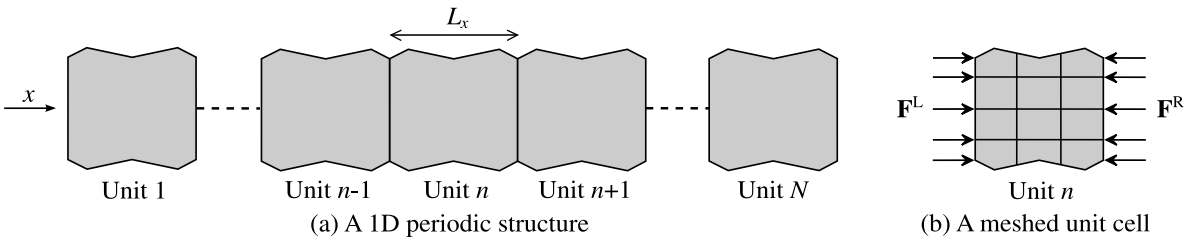

Fig. 3. One-dimensional periodic structure and its unit cells. The DOFs in a unit can be divided into left (L), internal (I), and right (R). L_x is the length of a unit cell along the x. N denotes the number of unit cells. **F** indicates the harmonic force on the boundary of the unit cell.

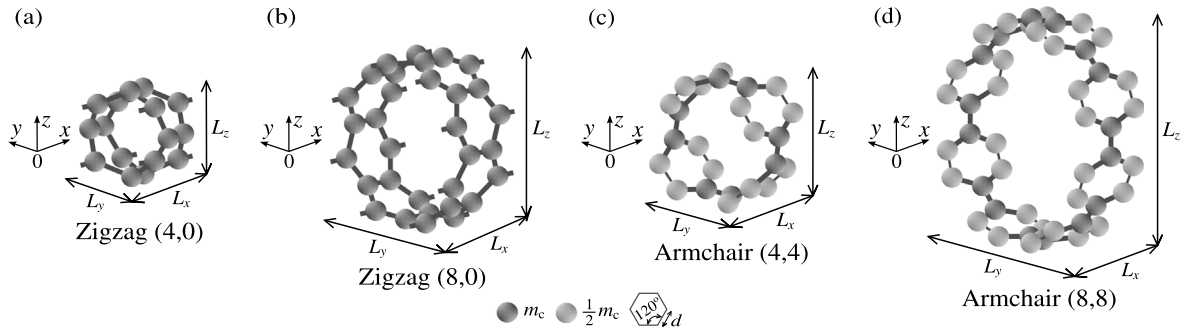

Fig. 4. Four different unit cells of CNTs. (a): A unit cell of zigzag (4,0) CNTs. (b): A unit cell of zigzag (8,0) CNTs. (c): A unit cell of armchair (4,4) CNTs. (d): A unit cell of armchair (8,8) CNTs.

measurement representing the distribution of modal natural frequencies in the frequency domain. Modal density of a structure at frequency ω, representing the number of resonant frequencies in a neighborhood $\Delta\omega$ local to that frequency, is expressed as: $D_m = \mathrm{d}N_m(\kappa)/\mathrm{d}\omega(\kappa)$, in which $N_m(\kappa)$, the number of resonant frequencies under the given frequency, can be written as $\mathrm{d}N_m(\kappa) = \kappa L_x/\pi$. Then, the modal density will be re-expressed as: $D_m = (L_x/\pi)(\mathrm{d}\kappa/\mathrm{d}\omega(\kappa))$.

4. Simulation results of CNTs

The investigation into the nonlinear properties of CNTs bears significance, as it furnishes essential insights for the application of CNT-based nanostructures within engineering domains. In this section, the dynamic phenomena encompassing dispersion relationships, modal density, forced response, and displacement fields are explicated.

As shown in Fig. 4, four different unit cells of CNTs are introduced, namely zigzag (4,0), zigzag (8,0), armchair (4,4), and armchair (8,8). The Young's modulus of σ-bond $E = 5.49 \times 10^{12}$ Pa according to Eq. (19), mass density $\rho = 2200$ kg/m^3, $d = 1.42$ Å (1 Å $= 1 \times 10^{-10}$ m), $L_x = 3d$, $L_y = \sqrt{3}d$, the cross-section radius of the σ-bond is $r = 0.733$ Å, the mass of a carbon atom $m = 1.99 \times 10^{-26}$ kg, damping loss factor $\eta = 1e^{-3}$. The parameters mentioned above can be found in [71,72,74].

4.1. Parameters study on a single beam

As depicted in Fig. 5, the investigation herein pertains to the influence of higher-order material and inertia parameters upon the stiffness and mass of a σ-bond beam as delineated by Eq. (12). In this study, each parameter is subjected to multiplication by a scalar factor, denoted as δ: $l_a = \delta l_p$, $l_b = \delta l_p$, $l_{b_1} = \delta l_p$, $l_c = \delta(l_p)^2$, $l_{c_1} = \delta(l_p)^2$, $l_1 = \delta l_p$, $l_2 = \delta l_p$, where length scale parameter l_p is chosen as $r/2.5$. The ensuing repercussions are examined across the spectrum of δ values ranging from −4 to 4. Here, when analyzing the effect of one parameter, the δ for the other parameters is kept as 1. Fig. 5(a) addresses the impact of higher-order material parameters (l_a, l_{a_1}, l_b, l_{b_1}, and l_c) on the linear stiffness. It elucidates that as the scalar factor δ increases, the values of linear stiffness initially exhibit a descending tendency, subsequently transitioning into an ascending trajectory. However, it is worth noting that in the case of parameter l_c, the linear stiffness consistently registers a decrement. An observation emerges when δ surpasses a threshold of 2.8, signifying that the linear stiffness attributed to l_c attains negative magnitudes. Fig. 5(b) depicts the impact of higher-order material parameters (l_a, l_b, and l_c) on nonlinear stiffness. Here, akin to the previous analysis, an analogous pattern manifests: as δ undergoes augmentation, the nonlinear stiffness initially embarks upon a declining trajectory, subsequently pivoting towards an upward trend. It is pertinent to mention that, similar to the linear stiffness case, parameter l_c consistently engenders a reduction in nonlinear stiffness. Furthermore, the result shows that when δ surpasses 1.6, the nonlinear stiffness attributed to l_c plunges into the domain of negative values. Similarly, the nonlinear stiffness pertaining to l_b assumes negative values within the interval of −0.7 to 0.7 for δ. Lastly, Fig. 5(c) expounds upon the impact of higher-order inertia parameters (l_1 and l_2) upon mass. The findings signify that as the scalar factor δ escalates, the mass initially experiences an augmentation, subsequently undergoing a decrement. It is imperative to emphasize that the higher-order material parameter l_b yields the most pronounced influence on stiffness when δ exceeds a threshold of 1. Simultaneously, the higher-order inertia parameter l_2 exerts the most significant impact on mass when δ surpasses the value of 1. In order to maintain the physical integrity of the stiffness values, it is required that $\delta > 0.7$ for l_b, and $\delta < 1.6$ for l_c. For the purposes of this study, the selection of higher-order parameters adheres to the following configurations: $\delta = 1$ for l_a, l_c, l_{c_1}, l_1, and l_2, $\delta = 2$ for l_b and l_{b_1}.

4.2. Wave propagation in CNTs

In this section, the focus shifts towards the exploration of the dispersion characteristics of CNTs in order to investigate their wave propagation behavior. As depicted in Fig. 6(a) and (b), the dispersion relation under low frequency for the zigzag (4,0) and zigzag (8,0) CNTs are presented, respectively. The continuous black lines represent outcomes derived from the linear SSG theory, while continuous red lines signify the results emanating from the nonlinear SSG framework. Meanwhile, dotted black lines correspond to the outcomes yielded by the linear CT. Evidently, with the increment of frequency, the disparities between the results produced by the SSG and CT methods

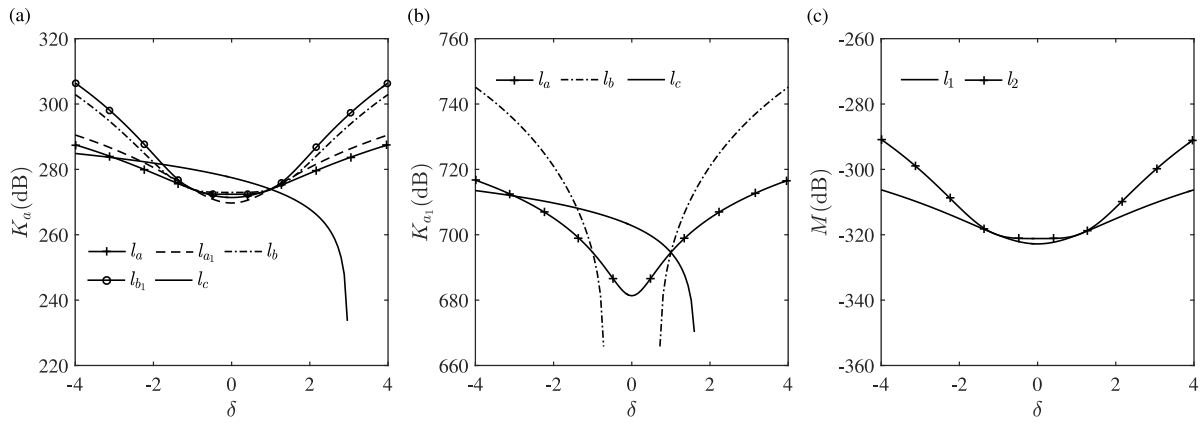

Fig. 5. The influence of higher-order material and inertia parameters on the stiffness and mass. (a): The influence of higher-order material parameters on the linear stiffness. (b): The influence of higher-order material parameters on the nonlinear stiffness. (c): The influence of higher-order inertia parameters on the mass.

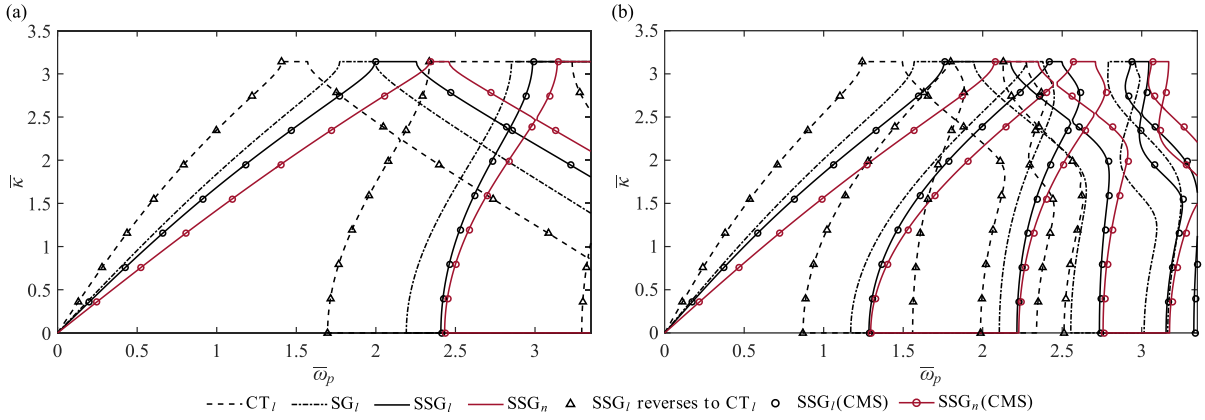

Fig. 6. The dispersion relation of zigzag CNTs under low frequency. (a): The dispersion relation of zigzag (4,0). (b): The dispersion relation of zigzag (8,0). $\overline{\kappa}$, denoting the normalized wavenumber, is defined as: $\overline{\kappa} = \kappa / L_x$, where L_x is the length of a unit cell along x direction. $\overline{\omega}_p$, representing the normalized frequency, can be defined as: $\overline{\omega}_p = \omega_p / \omega_p^0$, where ω_p^0 is the first natural frequency of a unit cell. $\overline{\omega}_p = \overline{\omega}_0$ indicates linear, $\overline{\omega}_p = \overline{\omega}$ means nonlinear.

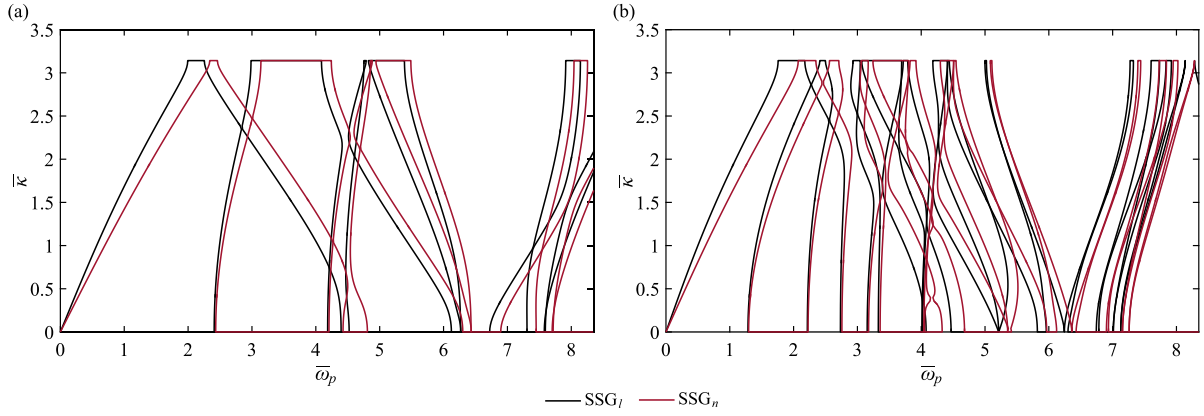

Fig. 7. The dispersion relation of zigzag CNTs under low and high frequencies using linear and nonlinear SSG theories. (a): The dispersion relation of zigzag (4,0). (b): The dispersion relation of zigzag (8,0). $\overline{\omega}_p = \overline{\omega}_0$ indicates linear, $\overline{\omega}_p = \overline{\omega}$ means nonlinear.

become increasingly noticeable. Moreover, it becomes apparent that the frequency values derived from the nonlinear SSG theory consistently surpass those originating from the CT, linear SG, and linear SSG theories at the same wavenumber values. This divergence can be attributed to the incorporation of a nonlinear component, involving the nonlinear Green–Lagrange strain tensor, consequently causing the eigenvalues to surpass those from the CT and linear SSG under the same wavenumber, thereby resulting in a stiffness hardening. On the other hand, at the same position in κ-space, the linear SSG exhibits a higher frequency value compared to CT. In SSG theory, the potential energy density is determined by strain, the first gradient of strain, and the second gradient of strain. Consequently, the dynamical equilibrium equation becomes a high-order partial differential function comprising classical and non-classical components in SSG theory. The presence of non-classical parts, which include higher-order parameters, results in the eigenvalue calculated by the dynamical equilibrium equation in SSG theory being greater than that in CT at the corresponding κ-space position. Furthermore, the frequency values determined through

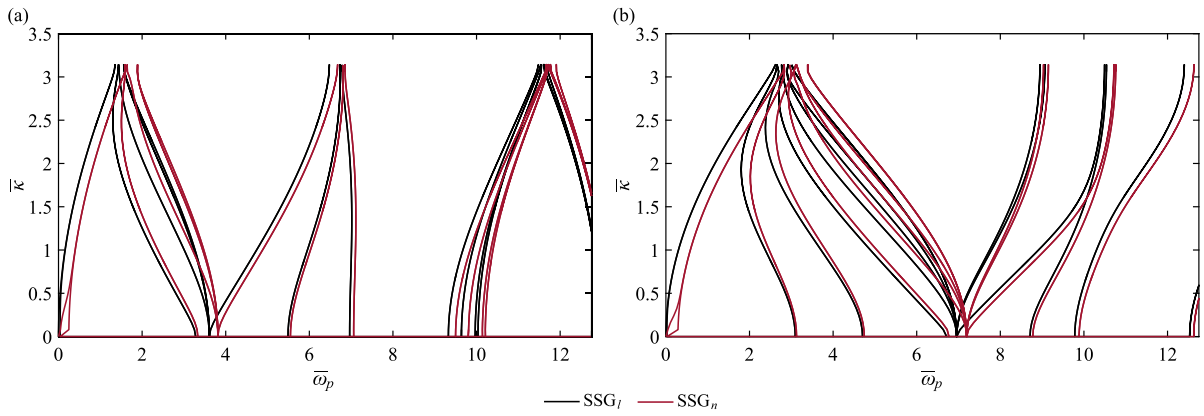

Fig. 8. The dispersion relation of armchair CNTs under low and higher frequencies using linear and nonlinear SSG theories. (a): The dispersion relation of armchair (4,4). (b): The dispersion relation of armchair (8,8). $\overline{\omega}_p = \overline{\omega}_0$ indicates linear, $\overline{\omega}_p = \overline{\omega}$ means nonlinear.

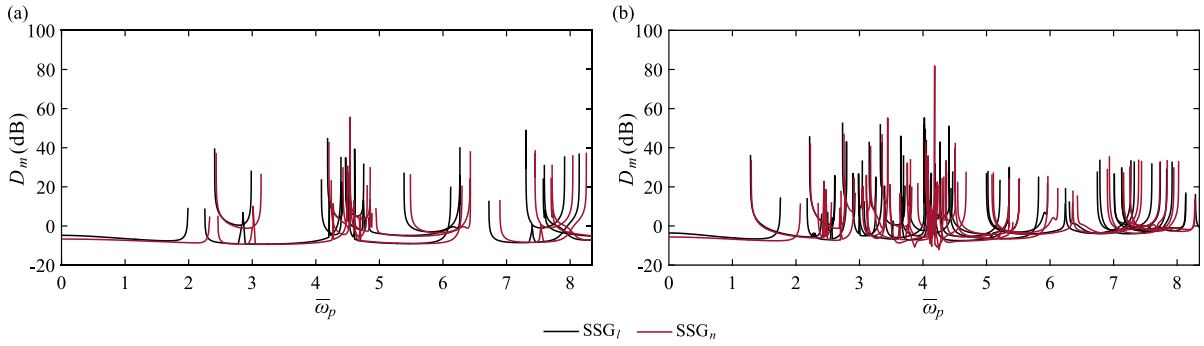

Fig. 9. The linear and nonlinear model density of zigzag CNTs. (a): The model density of zigzag (4,0). (b): The model density of zigzag (8,0). The continuous black lines represent outcomes derived from the linear SSG. The continuous red lines signify the results emanating from the nonlinear SSG.

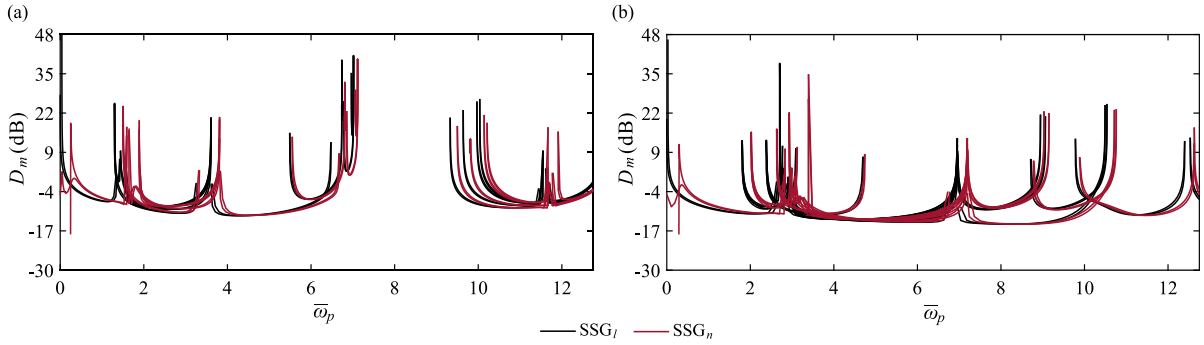

Fig. 10. The linear and nonlinear model density of armchair CNTs. (a): The model density of armchair (4,4). (b): The model density of armchair (8,8). The continuous black lines represent outcomes derived from the linear SSG. The continuous red lines signify the results emanating from the nonlinear SSG.

the linear SG approach are interposed between those obtained via the CT and linear SSG. Notably, the first stop band as identified through the nonlinear SSG is observed to be narrower than that identified by the linear SSG. It should be pointed out that the inclusion of transverse shear deformation in other beams, such as the Timoshenko beam, alters the dispersion relation, leading to a distinct conclusion compared to the one illustrated in Fig. 6. To validate the results under the SSG framework, a Component Mode Synthesis (CMS) method [75] is employed. The CMS results exhibit an alignment with the WFEM results. However, the CMS method demonstrates efficacy in simulating lower-order eigenvalues. Errors may manifest when computing higher-order eigenvalues. Additionally, in the limiting case where higher-order parameters are set to zero, the SSG theory converges towards the CT, which serves as a rational means to ascertain the accuracy of the simulation outcomes.

Fig. 7 depicts the dispersion relation under low and high frequencies for zigzag (4,0) and zigzag (8,0) CNTs, employing both linear and nonlinear SSG. A comparative analysis between the two theoretical frameworks shows that, as the normalized wave number approximates zero, the results obtained from the linear SSG approach closely align with those emanating from the nonlinear SSG theory, up to the first three branches for zigzag (4,0), but extend to the first six branches for zigzag (8,0). A noticeable discrepancy between the two manifests itself primarily when the normalized wavenumber nears π at low frequency. At elevated frequency, the disparity between linear and nonlinear SSG becomes pronounced across the entire wave propagation domain. Notably, the stop band phenomenon in zigzag (4,0) is both more conspicuous and wider in extent compared to that in zigzag (8,0). Furthermore, Fig. 8 provides an exposition of the dispersion relation under low and high frequencies for armchair (4,4) and armchair (8,8)

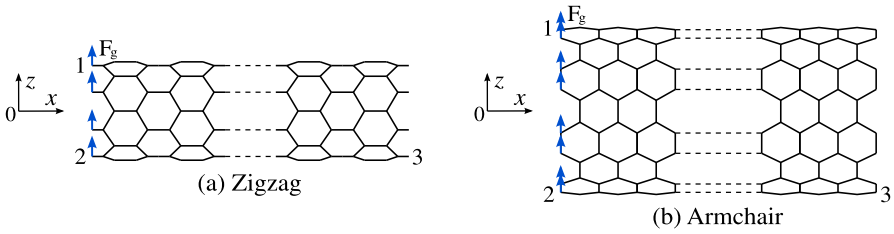

Fig. 11. The schematic of zigzag CNTs with 10 unit cells and armchair CNTs with 15 unit cells along x direction. The point forces are loaded on the left boundary of CNTs. There are two boundary conditions. 1: Points 2 and 3 are free (F-F). 2: Points 2 and 3 are clamped (C-C).

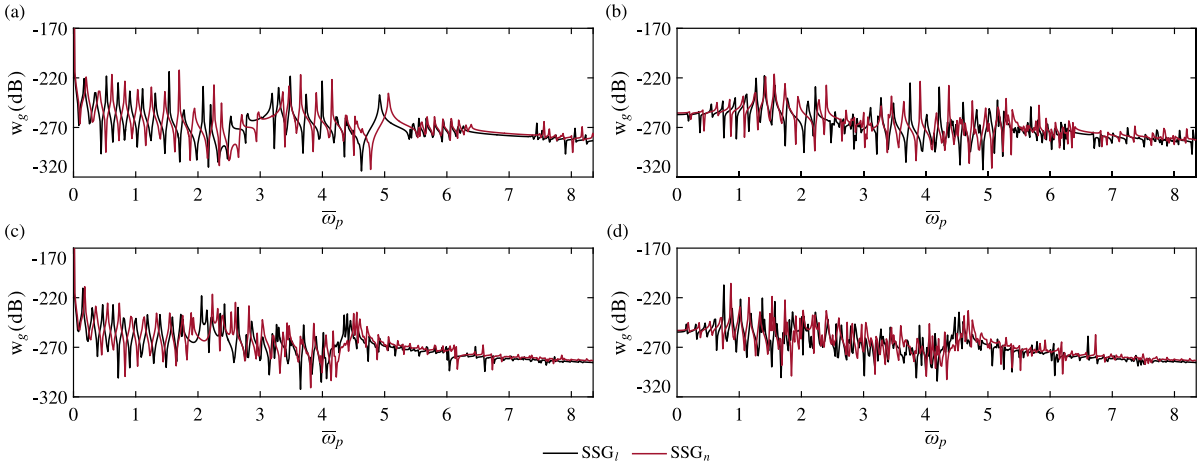

Fig. 12. Forced response of zigzag CNTs along z direction at point 1 using linear and nonlinear SSG theories. (a): Zigzag (4,0) with F-F boundary condition. (b): Zigzag (4,0) with C-C boundary condition. (c): Zigzag (8,0) with F-F boundary condition. (d): Zigzag (8,0) with C-C boundary condition.

CNTs within linear and nonlinear SSG methods. The results substantiate the existence of a pronounced stop band in armchair (4,4) when the normalized frequency lies within the range of 7 to 9. In contrast, no such stop band is discernible in armchair (8,8). This outcome underscores the superior wave-controlling efficacy of armchair (4,4) in comparison to armchair (8,8).

4.3. Modal density analysis

When subjected to high frequency excitation, a system may manifest a substantial presence of high-order modes within its response dynamics. Concurrently, within the elevated frequency regime, wavelengths tend to approximate the dimensions of internal micro-structures, thereby accentuating their discernible influence on the propagation of waves. The endeavor to model such systems invariably gives rise to the exigency of high frequency vibrational analysis, with Statistical Energy Analysis (SEA) emerging as one of the predominant methodologies for this purpose. In this section, a pivotal parameter intrinsic to the SEA methodology, specifically the modal density is considered in the investigation, as predicated upon the framework advanced herein. Fig. 9 illustrates the modal density characteristics of linear and nonlinear waves within the framework of the SSG theory, specifically applied to zigzag (4,0) and zigzag (8,0) CNTs. These findings are confined to the frequency domain, where discernible ramifications of geometric nonlinearity become evident. It is noteworthy that a substantial augmentation in modal density is observed proximate to the critical frequency regions, often referred to as the cut-on/off positions. Moreover, an examination of the modal density reveals that it almost remains invariant over the low frequency interval spanning from 0 to 1.8 for the linear zigzag (4,0) CNTs, and from 0 to 2.2 for the nonlinear zigzag (4,0) CNTs. Similarly, the modal density exhibits constancy in the frequency range from 0 to 1.6 for the linear zigzag (8,0) CNTs, and from 0 to 1.8 for the nonlinear zigzag (8,0) CNTs. A phase delay occurs between linear and nonlinear outcomes. This phenomenon can be explained as follows: the potential energy density in nonlinear SSG relies on the Green–Lagrange nonlinear strain, the first gradient of nonlinear strain, and the second gradient of nonlinear strain. The determination of frequency can be confirmed by combining the solutions related to the linear zero-order system and the perturbed system. Thus, the presence of the nonlinear component in frequency leads to a phase discrepancy between linear and nonlinear results. On other hand, Fig. 10 presents a comparative analysis of modal density pertaining to linear and nonlinear wave propagation employing the SSG theory, specifically applied to armchair (4,4) and armchair (8,8) CNTs. It is observed that the modal density of zigzag CNTs exhibits a notably smoother behavior across a broader spectrum in comparison to the armchair CNTs at low frequency. Evidently, an overt presence of a stop band is discerned in the modal density profile of armchair (4,4) CNTs, a phenomenon consistent with the findings elucidated in the previous section about dispersion relation, whereas no such stop band manifestation is evident in armchair (8,8) CNTs.

4.4. Forced response of CNTs

In the present section, an investigation into the dynamic characteristics of CNTs is undertaken, with a specific focus on elucidating the forced response of zigzag CNTs comprising 10 unit cells and armchair CNTs consisting of 15 unit cells along the x axis. The nonlinear forced response is mathematically articulated as: $\mathbf{D}_g\mathbf{w}_g = \mathbf{F}_g - \frac{3}{4}\mathbf{K}_{\mathrm{N}_g}\mathbf{w}_g^3$, where $\mathbf{w}_g$, representing the amplitude of the displacement vector of global structure, can be solved by Newton's method [76]. The matrix $\mathbf{D}_g$ is defined as $(1+i\eta)\mathbf{K}_g - \omega^2\mathbf{M}_g$, where $\mathbf{K}_g$ and $\mathbf{M}_g$ correspond to the global stiffness and mass matrices, respectively, both of which are constructed through the assembly of unit stiffness ($\mathbf{K}$) and mass ($\mathbf{M}$) matrices. $\mathbf{F}_g$ denotes the amplitude of the global force vector. As illustrated in Fig. 11, the harmonic point forces are applied to the left boundary

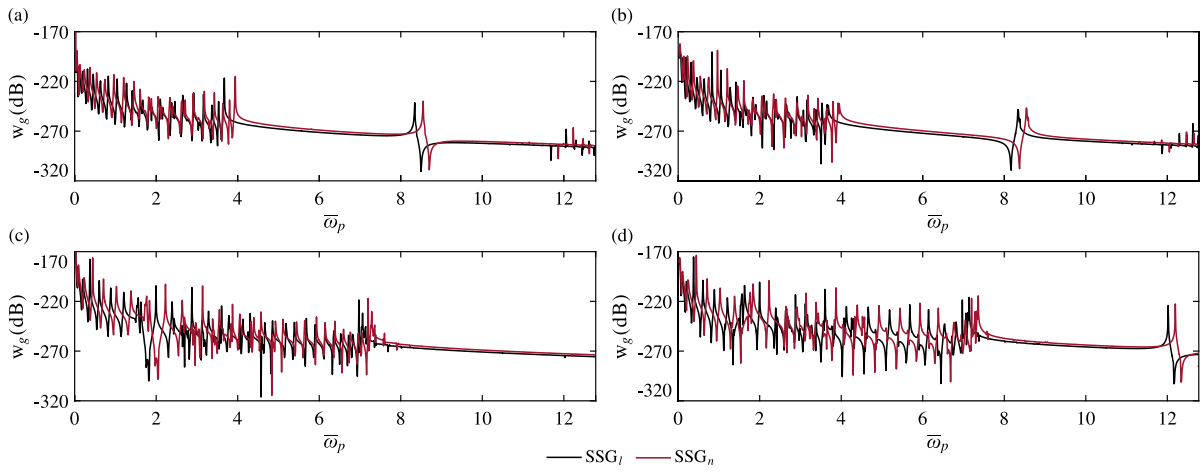

Fig. 13. Forced response of armchair CNTs along z direction at point 1 using linear and nonlinear SSG theories. (a): Armchair (4,4) with F-F boundary condition. (b): Armchair (4,4) with C-C boundary condition. (c): Armchair (8,8) with F-F boundary condition. (d): Armchair (8,8) with C-C boundary condition.

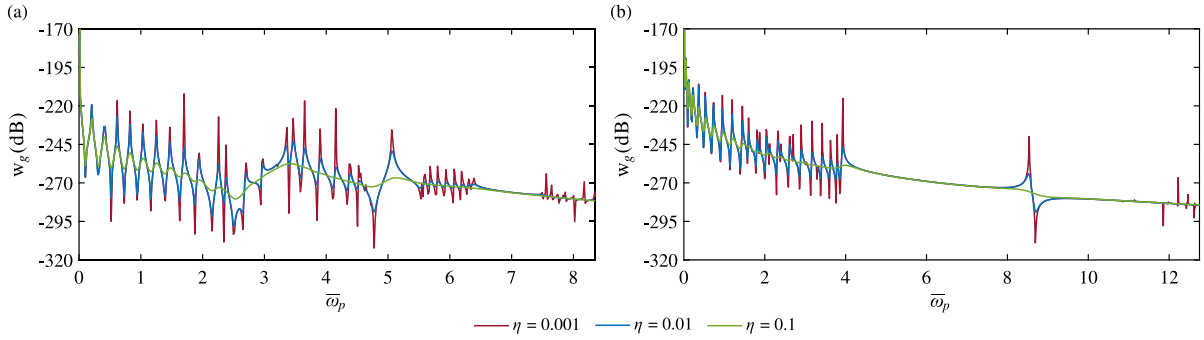

Fig. 14. The influence of damping loss on the forced response by nonlinear SSG theory. (a): Zigzag (4,0) with F-F boundary condition. (b): Armchair (4,4) with F-F boundary condition. The continuous red lines represent outcomes when $\eta = 0.001$. The continuous blue lines signify the results when $\eta = 0.01$. The continuous green lines denote the results when $\eta = 0.1$.

of the CNTs. Two distinct boundary conditions are considered: firstly, a free–free (F-F) condition, wherein points 2 and 3 are free, and secondly, a clamped–clamped (C–C) condition, wherein points 2 and 3 are clamped. Consequently, the forced response at point 1 is calculated based on the different boundary conditions imposed. Fig. 12(a)–(d) exhibit the forced responses of zigzag CNTs under two boundary conditions, specifically, F-F and C-C boundary conditions for both zigzag (4,0) and zigzag (8,0). It is evident that the resonant behaviors are aptly anticipated in both linear and nonlinear SSG theories. In agreement with the trends observed in dispersion curves, the outcomes reveal a progressive escalation in the disparities between linear and nonlinear SSG theories as the excitation frequency undergoes augmentation. This phenomenon underscores the profound influence of geometric nonlinearity on wave propagation characteristics. Pertinently, the vibrational energy input is capable of dual modes of transmission: propagation wave and evanescent waves, which, notably, evince rapid decay within the immediate vicinity of the excitation source.

What is more, Fig. 13(a)–(d) delineate the forced responses of armchair CNTs characterized by two boundary conditions: armchair (4,4) and armchair (8,8) under the F-F boundary condition, armchair (4,4) and armchair (8,8) under the C-C boundary condition. Notably deviating from the vibrational responses observed in zigzag CNTs, the results of the armchair CNTs' forced responses exhibit heightened smoothness, particularly in the realm of high frequency. These armchair CNTs exhibit minimal vibrational excitation at high frequency, indicative of their robust wave controlling capabilities. It can be noticed that resonances are predicted in both linear and nonlinear theories. A comparison between the linear SSG and the nonlinear SSG reveals that, at low frequencies, the forced response by the linear SSG aligns with the nonlinear SSG. However, similar to the dispersion curves, discrepancies in forced responses between the linear SSG and the nonlinear SSG become more pronounced as the frequency increases. The nonlinear components in the SSG theory can impact wave propagation. The input vibration energy is transferred through both propagating waves and evanescent waves, which rapidly decay in the near field of the excitation. Additionally, with increasing frequency, the dissipation of vibrational energy becomes noticeably more obvious when compared to zigzag CNTs.

On the other hand, the present discourse centers on the exploration of damping loss impact on the forced response. As depicted in Fig. 14, the nonlinear forced response is delineated for both zigzag (4,0) and armchair (4,4) CNTs, each subject to the F-F boundary conditions. It is noteworthy that the damping loss factor, denoted as η, is varied across three values: 0.001, 0.01, and 0.1. It is imperative to underscore that augmented damping exerts a discernible inhibitory effect upon vibrational modes proximate to the stop band, thereby leading to a substantial expansion of the controlled bandwidth.

An alternative approach for comprehending the dynamic characteristics inherent to CNTs resides in the analysis of the displacement field. As illustrated in Fig. 15, the vertical displacement field of a zigzag (8,0) CNT subject to the C-C boundary is depicted, employing both linear and nonlinear SSG theories. Here, three normalized frequencies are selected, namely 0.5, 1.5, and 2.8. It is discernible that when the frequencies assume values of 0.5 and 1.5, residing within the pass band regime, the CNT structure manifests vibrational behavior. However, when the frequency attains the value of 2.8, corresponding to the stop band frequency, vibrational activity ceases within the structure when employing linear SSG, but a residual weak vibrational response

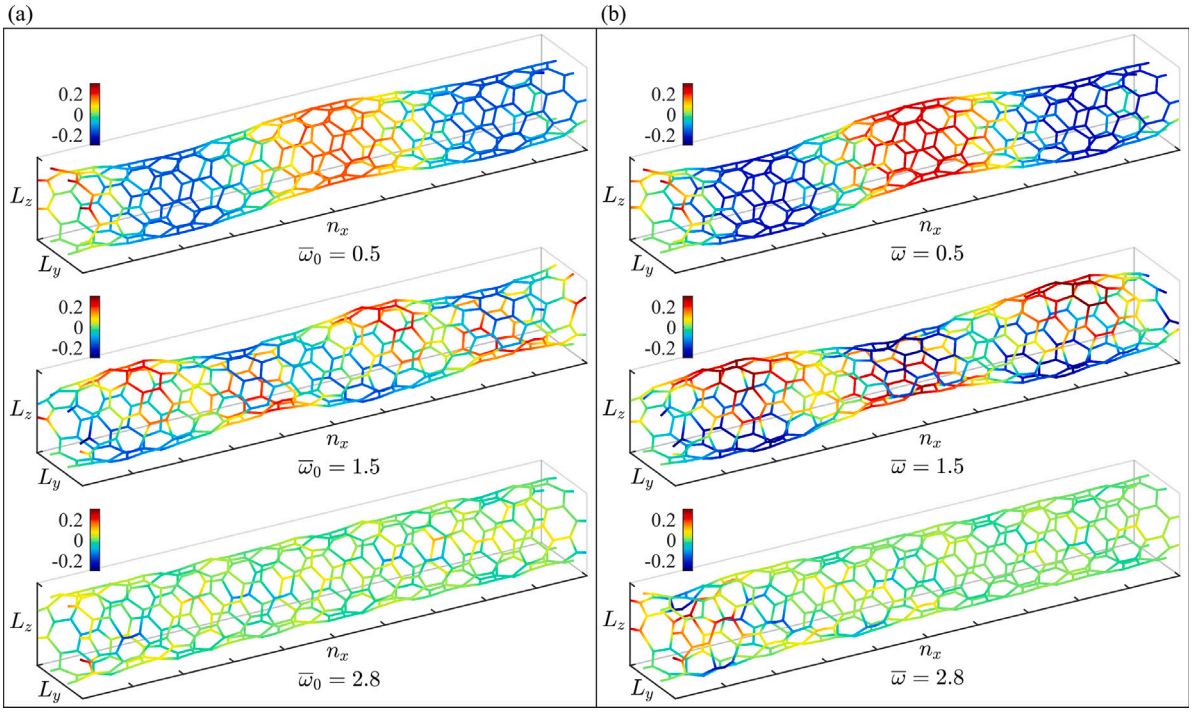

Fig. 15. The displacement field of zigzag (8,0) CNTs along z direction with the chosen frequencies under C-C boundary condition by linear and nonlinear SSG theories. (a): Linear displacement field. (b): Nonlinear displacement field.

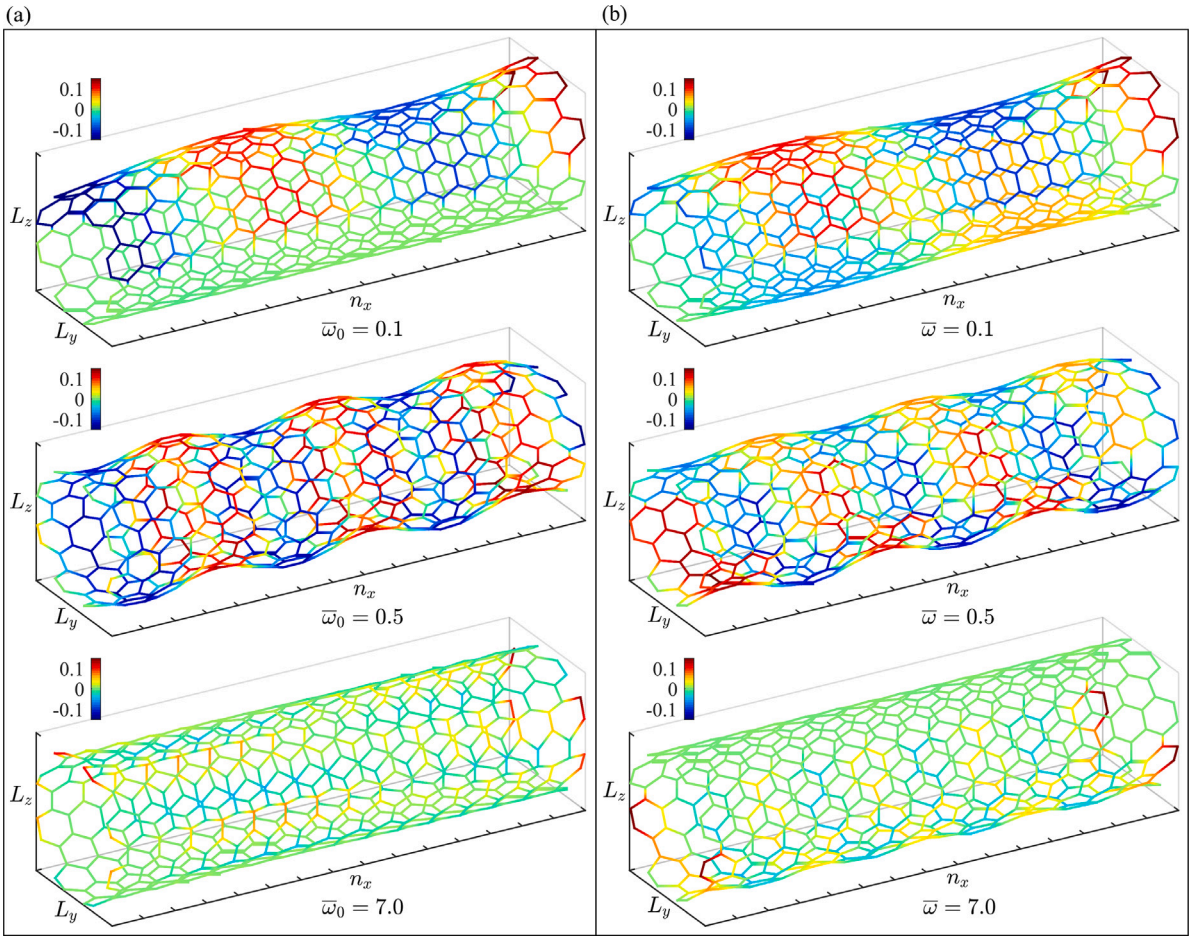

Fig. 16. The displacement field of armchair (8,8) CNTs along z direction with the chosen frequencies under C-C boundary condition by linear and nonlinear SSG theories. (a): Linear displacement field. (b): Nonlinear displacement field.

exists under the nonlinear SSG. At the low frequency, such as 0.5, the nonlinear SSG results in a greater displacement amplitude compared to the linear SSG. At the middle frequency, such as 1.5, the linear SSG produces the highest displacement amplitude on the left and middle of the structure, whereas the nonlinear SSG places it on the left and right. The presence of nonlinearity not only influences the peak displacement value but also influences the deformed position of the structure. On the other hand, in Fig. 16, the illustration portrays the vertical displacement field within an armchair (8,8) CNT subjected to the C-C boundary condition. This depiction is achieved by employing both linear and nonlinear SSG theories. Notably, the graphic demonstrates that at low frequency, specifically at 0.1, the vibrational response is predominantly localized at the top of the CNT structure as predicted by the linear SSG theory. Concurrently, nonlinear SSG theory predicts a weak vibration phenomenon occurring at the bottom of the CNT structure. In congruence with analogous findings in the context of zigzag CNTs, it is observed that when the frequency reaches the stop band regime or point, exemplified by 7.0, the linear SSG theory can anticipate a structural response, characterized by an absence of vibration. However, the nonlinear SSG theory unveils the persistence of a feeble vibrational mode localized at the bottom of the CNT structure under these frequency conditions.

5. Conclusions

This study explores the geometrically nonlinear dynamic characteristics inherent in carbon nanotubes (CNTs), incorporating size effects through SSG elasticity. Given the significance of size effects in CNT behavior, capturing these effects is crucial for precise applications. To achieve this goal, we introduce strain–displacement relationships that account for geometric nonlinearity, rooted in the SSG theory. The formulation of governing equations and boundary conditions is accomplished through proper dimension reduction applied to Hamilton's principle. Following the derivation of weak formulation and finite element matrices, we introduce a perturbation methodology that integrates nonlinear phenomena into the context of linear wave propagation within the framework of periodic structures theory.

Subsequently, we present an investigation of the dispersion relation of CNTs. A comparative analysis is carried out between frequency values obtained using the nonlinear SSG theory and those derived from the linear CT, SG, and SSG theories. It is observed that the nonlinear SSG theory generates frequency values of greater magnitude compared to the linear CT and SSG theories. This discrepancy in results provides an explanation for the presence of stiffness hardening in CNTs. The introduction of a nonlinear component in the formulation of strain energy density emerges as a significant factor contributing to the increase in frequency values in nonlinear results as opposed to linear outcomes. The impact of higher-order parameters on both stiffness and mass characteristics is investigated. Notably, the higher-order material parameter l_b and higher-order inertia parameter l_2 exert the most pronounced influence on stiffness and mass, respectively. In comparison between zigzag and armchair CNTs, the study reveals that armchair CNTs exhibit superior wave control properties.

Furthermore, a study of the forced response of CNTs is conducted under different boundary conditions. It becomes evident that resonant phenomena can be anticipated in both linear and nonlinear SSG theories. The input vibrational energy can be conveyed through dual modes, specifically propagating waves and evanescent waves, which exhibit rapid decay near the excitation source. With increasing frequency, the dissipation of vibrational energy in armchair CNTs becomes notably more pronounced compared to zigzag CNTs. It is clear that, within the pass band regime, the CNT structure demonstrates vibrational behavior. However, when the frequency reaches the value corresponding to the stop band frequency, vibrational activity ceases within the structure when utilizing linear SSG, but a feeble vibrational response persists under the framework of nonlinear SSG.

CRediT authorship contribution statement

Bo Yang: Data curation, Investigation, Methodology, Software, Validation, Visualization, Writing – original draft, Writing – review & editing. **Mahmoud Mousavi:** Conceptualization, Formal analysis, Funding acquisition, Project administration, Supervision, Writing – review & editing.

Declaration of competing interest

The authors declare that they have no known competing financial interests or personal relationships that could have appeared to influence the work reported in this paper.

Data availability

No data was used for the research described in the article.

Acknowledgments

The authors benefited from discussions with Arash Yavari. This work is funded by the European Union's Horizon Europe Programme (NANOWAVE) under the Marie Skłodowska-Curie Actions grant agreement No. 101105373.

Appendix A. Definitions of G, G_a, G_b, G_c and G_0 in Eq. (7)

$$
\begin{aligned}
G = \int_0^{d_L} \Bigg[& \frac{1}{4}\frac{A}{I}\left(\frac{\partial w(\overline{x},t)}{\partial \overline{x}}\right)^4 + l_a^2\frac{A}{I}\left(\frac{\partial w(\overline{x},t)}{\partial \overline{x}}\frac{\partial^2 w(\overline{x},t)}{\partial \overline{x}^2}\right)^2 \\
& + l_b^4\frac{A}{I}\Bigg(\left(\frac{\partial^2 w(\overline{x},t)}{\partial \overline{x}^2}\right)^2 \\
& + \frac{\partial w(\overline{x},t)}{\partial \overline{x}}\frac{\partial^3 w(\overline{x},t)}{\partial^3 \overline{x}}\Bigg)^2 + l_c\frac{A}{I}\left(\frac{\partial w(\overline{x},t)}{\partial \overline{x}}\right)^2 \\
& \times\left(\left(\frac{\partial^2 w(\overline{x},t)}{\partial \overline{x}^2}\right)^2 + \frac{\partial w(\overline{x},t)}{\partial \overline{x}}\frac{\partial^3 w(\overline{x},t)}{\partial^3 \overline{x}}\right) \\
& + \left(1 + l_{a_1}^2\frac{A}{I}\right)\left(\frac{\partial^2 w(\overline{x},t)}{\partial \overline{x}^2}\right)^2\Bigg] \mathrm{d}\overline{x},
\end{aligned}
\tag{A.1}
$$

$$
G_a = \int_0^{d_L}\left(\frac{\partial^3 w(\overline{x},t)}{\partial \overline{x}^3}\right)^2 \mathrm{d}\overline{x}, \quad G_b = \int_0^{d_L}\left(\frac{\partial^4 w(\overline{x},t)}{\partial \overline{x}^4}\right)^2 \mathrm{d}\overline{x},
$$

$$
G_c = \int_0^{d_L} 2\frac{\partial^2 w(\overline{x},t)}{\partial \overline{x}^2}\frac{\partial^4 w(\overline{x},t)}{\partial \overline{x}^4}\mathrm{d}\overline{x},
$$

$$
G_0 = \int_0^{d_L}\left[\left(\frac{\partial^2 w(\overline{x},t)}{\partial \overline{x}^2}\right)^2 + \frac{\partial w(\overline{x},t)}{\partial \overline{x}}\frac{\partial^3 w(\overline{x},t)}{\partial^3 \overline{x}}\right]\mathrm{d}\overline{x},
$$

Appendix B. Expressions of boundary conditions

$$
\begin{aligned}
& \Bigg\{ -\frac{1}{2}EA\left[\left(\frac{\partial w(\overline{x},t)}{\partial \overline{x}}\right)^2 - \left(l_a^2 - 2l_c\right)\frac{\partial^2}{\partial x^2}\left(\frac{\partial w(\overline{x},t)}{\partial \overline{x}}\right)^2\right. \\
& \quad \left. + l_b^4\frac{\partial^4}{\partial x^4}\left(\frac{\partial w(\overline{x},t)}{\partial \overline{x}}\right)^2\right]\frac{\partial w(\overline{x},t)}{\partial \overline{x}} \\
& + EI\left[\left(1 + \frac{A}{I}l_{a_1}^2\right)\frac{\partial^3 w(\overline{x},t)}{\partial \overline{x}^3} - \left(l_a^2 + \frac{A}{I}l_{b_1}^4 - 2l_c\right)\frac{\partial^5 w(\overline{x},t)}{\partial \overline{x}^5} + l_b^4\frac{\partial^7 w(\overline{x},t)}{\partial \overline{x}^7}\right] \\
& - \rho\left(\left(I + Al_1^2\right)\frac{\partial^3 w(\overline{x},t)}{\partial \overline{x}\partial t^2} - \left(Il_1^2 + Al_2^4\right)\frac{\partial^5 w(\overline{x},t)}{\partial \overline{x}^3\partial t^2} + Il_2^4\frac{\partial^7 w(\overline{x},t)}{\partial \overline{x}^5\partial t^2}\right) \\
& \quad + f_0\Bigg\}\Bigg|_0^{d_L} = 0 \\
& \text{or } \delta w(\overline{x},t) = 0, \text{ for } \overline{x} = \{0, d_L\},
\end{aligned}
\tag{B.1}
$$

$$\left\{-EI\left[\left(1+\frac{A}{I}l_{a_1}^2\right)\frac{\partial^2 w(\bar{x},t)}{\partial\bar{x}^2}-\left(l_a^2+\frac{A}{I}l_{b_1}^4-2l_c\right)\frac{\partial^4 w(\bar{x},t)}{\partial\bar{x}^4}+l_b^4\frac{\partial^6 w(\bar{x},t)}{\partial\bar{x}^6}\right]-\rho\left(\left(Il_1^2+Al_2^4\right)\frac{\partial^4 w(\bar{x},t)}{\partial\bar{x}^2\partial t^2}-Il_2^4\frac{\partial^6 w(\bar{x},t)}{\partial\bar{x}^4\partial t^2}\right)+f_1\right\}\Big|_0^{d_L}=0 \text{ or } \delta\frac{\partial w(\bar{x},t)}{\partial\bar{x}}=0,\ \text{for } \bar{x}=\{0,d_L\}, \tag{B.2}$$

$$\left\{-EI\left[\left(l_a^2+\frac{A}{I}l_{b_1}^4-l_c\right)\frac{\partial^3 w(\bar{x},t)}{\partial\bar{x}^3}-l_b^4\frac{\partial^5 w(\bar{x},t)}{\partial\bar{x}^5}\right]-\rho Il_2^4\frac{\partial^5 w(\bar{x},t)}{\partial\bar{x}^3\partial t^2}+f_2\right\}\Big|_0^{d_L}=0 \text{ or } \delta\frac{\partial^2 w(\bar{x},t)}{\partial\bar{x}^2}=0,\ \text{for } \bar{x}=\{0,d_L\}, \tag{B.3}$$

$$\left\{-EI\left(l_c\frac{\partial^2 w(\bar{x},t)}{\partial\bar{x}^2}+l_b^4\frac{\partial^4 w(\bar{x},t)}{\partial\bar{x}^4}\right)+f_3\right\}\Big|_0^{d_L}=0 \text{ or } \delta\frac{\partial^3 w(\bar{x},t)}{\partial\bar{x}^3}=0,\ \text{for } \bar{x}=\{0,d_L\}. \tag{B.4}$$

Appendix C. Definitions of H_1, H_2, H_3, H_4, H_5, H_6, H_7, and H_8 in Eq. (11)

$$H_1=\frac{\partial^4 w(\bar{x},t)}{\partial\bar{x}^4},\ H_2=\frac{\partial^6 w(\bar{x},t)}{\partial\bar{x}^6},\ H_3=\frac{\partial^8 w(\bar{x},t)}{\partial\bar{x}^8}, \tag{C.1}$$

$$H_4=\frac{3}{2}\left(\frac{\partial w(\bar{x},t)}{\partial\bar{x}}\right)^2\frac{\partial^2 w(\bar{x},t)}{\partial\bar{x}^2}, \tag{C.2}$$

$$H_5=4\frac{\partial w(\bar{x},t)}{\partial\bar{x}}\frac{\partial^2 w(\bar{x},t)}{\partial\bar{x}^2}\frac{\partial^3 w(\bar{x},t)}{\partial\bar{x}^3}+\left(\frac{\partial^2 w(\bar{x},t)}{\partial\bar{x}^2}\right)^3+\left(\frac{\partial w(\bar{x},t)}{\partial\bar{x}}\right)^2\frac{\partial^4 w(\bar{x},t)}{\partial\bar{x}^4},$$

$$H_6=10\frac{\partial w(\bar{x},t)}{\partial\bar{x}}\frac{\partial^3 w(\bar{x},t)}{\partial\bar{x}^3}\frac{\partial^4 w(\bar{x},t)}{\partial\bar{x}^4}+3\left(\frac{\partial^3 w(\bar{x},t)}{\partial\bar{x}^3}\right)^2\frac{\partial^2 w(\bar{x},t)}{\partial\bar{x}^2}+4\left(\frac{\partial^2 w(\bar{x},t)}{\partial\bar{x}^2}\right)^2\frac{\partial^4 w(\bar{x},t)}{\partial\bar{x}^4}+6\frac{\partial w(\bar{x},t)}{\partial\bar{x}}\frac{\partial^2 w(\bar{x},t)}{\partial\bar{x}^2}\frac{\partial^5 w(\bar{x},t)}{\partial\bar{x}^5}+\left(\frac{\partial w(\bar{x},t)}{\partial\bar{x}}\right)^2\frac{\partial^6 w(\bar{x},t)}{\partial\bar{x}^6}, \tag{C.3}$$

$$H_7=\left(1+\frac{A}{I}l_1^2\right)\frac{\partial^4 w(\bar{x},t)}{\partial\bar{x}^2\partial t^2}-\left(l_1^2+\frac{A}{I}l_2^4\right)\frac{\partial^6 w(\bar{x},t)}{\partial\bar{x}^4\partial t^2}+l_2^4\frac{\partial^8 w(\bar{x},t)}{\partial\bar{x}^6\partial t^2},\quad H_8=\frac{\partial^2 w(\bar{x},t)}{\partial t^2}. \tag{C.4}$$

Appendix D. Derivation of perturbed system

The representation of the nodal displacement vector of a unit cell can be articulated as follows:

$$\begin{pmatrix}\hat{\mathbf{w}}_0^{\mathrm{L}}\\ \hat{\mathbf{w}}_0^{\mathrm{R}}\\ \hat{\mathbf{w}}_0^{\mathrm{I}}\end{pmatrix}=\begin{bmatrix}\mathbf{I}_{\mathrm{b}} & \mathbf{0}\\ e^{-\mathrm{i}\kappa L_x}\mathbf{I}_{\mathrm{b}} & \mathbf{0}\\ \mathbf{0} & \mathbf{I}_{\mathrm{i}}\end{bmatrix}\begin{pmatrix}\hat{\mathbf{w}}_0^{\mathrm{L}}\\ \hat{\mathbf{w}}_0^{\mathrm{I}}\end{pmatrix}, \tag{D.1}$$

where $\mathbf{I}_{\mathrm{b}}$ and $\mathbf{I}_{\mathrm{i}}$ indicate the identity matrix of size s and i, respectively. On the other hand, the nodal forces can adopt the following form:

$$\begin{pmatrix}\hat{\mathbf{w}}_0^{\mathrm{L}} & \hat{\mathbf{w}}_0^{\mathrm{I}}\end{pmatrix}\begin{bmatrix}e^{-\mathrm{i}\kappa L_x}\mathbf{I}_{\mathrm{b}} & \mathbf{I}_{\mathrm{b}} & \mathbf{0}\\ \mathbf{0} & \mathbf{0} & \mathbf{I}_{\mathrm{i}}\end{bmatrix}\begin{pmatrix}\hat{\mathbf{F}}^{\mathrm{L}}\\ \hat{\mathbf{F}}^{\mathrm{R}}\\ \mathbf{0}\end{pmatrix}=0. \tag{D.2}$$

Then, combining Eqs. (25), (D.1), and (D.2), this yields:

$$\hat{\mathbf{w}}_0^{\mathrm{b}\top}\mathbf{T}_1\left[(1+\mathrm{i}\eta)\mathbf{K}-\omega_0^2\mathbf{M}\right]\mathbf{T}_2\hat{\mathbf{w}}_0^{\mathrm{b}}=0, \tag{D.3}$$

where $\hat{\mathbf{w}}_0^{\mathrm{b}}=\left(\hat{\mathbf{w}}_0^{\mathrm{L}\top}\ \hat{\mathbf{w}}_0^{\mathrm{I}\top}\right)^\top$. $\mathbf{T}_1$ and $\mathbf{T}_2$ are given as:

$$\mathbf{T}_1=\begin{bmatrix}e^{-\mathrm{i}\kappa L_x}\mathbf{I}_{\mathrm{b}} & \mathbf{I}_{\mathrm{b}} & \mathbf{0}\\ \mathbf{0} & \mathbf{0} & \mathbf{I}_{\mathrm{i}}\end{bmatrix},\ \mathbf{T}_2=\begin{bmatrix}\mathbf{I}_{\mathrm{b}} & \mathbf{0}\\ e^{-\mathrm{i}\kappa L_x}\mathbf{I}_{\mathrm{b}} & \mathbf{0}\\ \mathbf{0} & \mathbf{I}_{\mathrm{i}}\end{bmatrix}. \tag{D.4}$$

To solve Eq. (D.3), a methodology is employed that entails a fixed value upon the wavenumber κ, thereby facilitating the determination of the associated set of ω_0 in an ascending sequence: $\omega_{0(1,\ldots,m)}^{i}$, where i indicates the ith element within the wavenumber spectrum, and m represents the mth component under the ith wavenumber. Additionally, the cut-on(off) frequency $\omega_{0(c)}$ is introduced as:

$$\begin{aligned}&(1+\mathrm{i}\eta)\left(\mathbf{K}^{\mathrm{LL}}+\lambda^{-1}\mathbf{K}^{\mathrm{RL}}+\lambda\mathbf{K}^{\mathrm{LR}}+\mathbf{K}^{\mathrm{RR}}\right)\hat{\mathbf{w}}_0^{\mathrm{L}}\\ &=\omega_{0(c)}^2\left(\mathbf{M}^{\mathrm{LL}}+\lambda^{-1}\mathbf{M}^{\mathrm{RL}}+\lambda\mathbf{M}^{\mathrm{LR}}+\mathbf{M}^{\mathrm{RR}}\right)\hat{\mathbf{w}}_0^{\mathrm{L}},\\ &(1+\mathrm{i}\eta)\left(\mathbf{K}^{\mathrm{LI}}+\lambda^{-1}\mathbf{K}^{\mathrm{RI}}\right)\hat{\mathbf{w}}_0^{\mathrm{I}}=\omega_{0(c)}^2\left(\mathbf{M}^{\mathrm{LI}}+\lambda^{-1}\mathbf{M}^{\mathrm{RI}}\right)\hat{\mathbf{w}}_0^{\mathrm{I}},\end{aligned} \tag{D.5}$$

where $\lambda=1$ or $\lambda=e^{-\mathrm{i}\pi L_x}$. $\hat{\mathbf{w}}_0^{\mathrm{L}}$ and $\hat{\mathbf{w}}_0^{\mathrm{I}}$ are the left and internal wave shapes of the unit cell. Next, submitting Eq. (D.1) into the part of $\mathbf{w}_0$ in Eq. (21), and doing the same calculation on $\mathbf{w}_1$, one arrives:

$$\hat{\mathbf{w}}_0=\mathbf{T}_2\hat{\mathbf{w}}_0^{\mathrm{b}},\ \hat{\mathbf{w}}_1=\mathbf{T}_2\hat{\mathbf{w}}_1^{\mathrm{b}}. \tag{D.6}$$

Subsequently, upon incorporating Eq. (D.6) into $\circ(\alpha^1)$ within Eq. (24), we have:

$$\circ(\alpha^1):\ \hat{\mathbf{w}}_1^{\mathrm{b}\top}\mathbf{T}_1\left[(1+\mathrm{i}\eta)\mathbf{K}-\omega_0^2\mathbf{M}\right]\mathbf{T}_2\hat{\mathbf{w}}_1^{\mathrm{b}}=2\omega_0\omega_1\hat{\mathbf{w}}_1^{\mathrm{b}\top}\mathbf{T}_1\mathbf{M}\mathbf{T}_2\hat{\mathbf{w}}_0^{\mathrm{b}}-\frac{3}{4}\hat{\mathbf{w}}_1^{\mathrm{b}\top}\mathbf{T}_1\boldsymbol{\mathcal{K}}_{\mathrm{N}}\left(\mathbf{T}_2\hat{\mathbf{w}}_0^{\mathrm{b}}\right)^3. \tag{D.7}$$

The eigenvector pertaining to the left-hand side of Eq. (D.7) corresponds precisely to that of Eq. (D.3), denoted as $\hat{\mathbf{w}}_1^{\mathrm{b}}=\hat{\mathbf{w}}_0^{\mathrm{b}}=\mathrm{X}_0^{\mathrm{b}}\boldsymbol{\Psi}_0^{\mathrm{b}}$. Consequently, Eq. (D.7) can be reformulated as follows:

$$8\omega_0\omega_1\boldsymbol{\Psi}_0^{\mathrm{b}\top}\mathbf{T}_1\mathbf{M}\mathbf{T}_2\boldsymbol{\Psi}_0^{\mathrm{b}}-3\mathrm{X}_0^{\mathrm{b}2}\boldsymbol{\Psi}_0^{\mathrm{b}\top}\mathbf{T}_1\boldsymbol{\mathcal{K}}_{\mathrm{N}}\left(\mathbf{T}_2\boldsymbol{\Psi}_0^{\mathrm{b}}\right)^3=0. \tag{D.8}$$

Finally, frequency ω_1 can be confirmed from Eq. (D.8).

References

[1] Shin DH, Kim H, Kim SH, Cheong H, Steeneken PG, Joo C, Lee SW. Graphene nano-electromechanical mass sensor with high resolution at room temperature. Iscience 2023;26(2).

[2] Hierold C, Jungen A, Stampfer C, Helbling T. Nano electromechanical sensors based on carbon nanotubes. Sensors Actuators A 2007;136(1):51–61.

[3] Chaudhary T, Siddiquee AN, Chanda AK, Abidi MH, Al-Ahmari A. Multi-response optimization for nimonic alloy miniature gear fabrication using wire electrical discharge machining. Adv Mech Eng 2020;12(10):1687814020967580.

[4] Desai S, Pandya A, Bhojawala V, Jha PK. Theoretical modelling of graphene system for nano-electromechanical resonator and force sensor. Phys E: Low-Dimens Syst Nanostruct 2023;147:115606.

[5] Tavakoli H, Mohammadi S, Li X, Fu G, Li X. Microfluidic platforms integrated with nano-sensors for point-of-care bioanalysis. TRAC Trends Anal Chem 2022;116806.

[6] Norizan MN, Moklis MH, Demon SZN, Halim NA, Samsuri A, Mohamad IS, Knight VF, Abdullah N. Carbon nanotubes: Functionalisation and their application in chemical sensors. RSC Adv 2020;10(71):43704–32.

[7] Kumar A, Sharma K, Dixit AR. A review on the mechanical properties of polymer composites reinforced by carbon nanotubes and graphene. Carbon Lett 2021;31(2):149–65.

[8] Sankapal BR, Gajare HB, Karade SS, Salunkhe RR, Dubal DP. Zinc oxide encapsulated carbon nanotube thin films for energy storage applications. Electrochim Acta 2016;192:377–84.

[9] Graham-Brady L, Arwade S, Corr D, Gutierrez M, Breysse D, Grigoriu M, Zabaras N. Probability and materials: from nano-to macro-scale: a summary. Probab Eng Mech 2006;21(3):193–9.

[10] VanLandingham M, Dagastine R, Eduljee R, McCullough R, Gillespie Jr J. Characterization of nanoscale property variations in polymer composite systems: 1. Experimental results. Compos A: Appl Sci Manuf 1999;30(1):75–83.

[11] Faleh NM, Fenjan RM, Ahmed RA. Forced vibrations of multi-phase crystalline porous shells based on strain gradient elasticity and pulse load effects. J Vib Eng Technol 2020;8(6):925–33.

[12] Lazar M, Maugin GA, Aifantis EC. Dislocation in second strain gradient elasticity. Int J Solids Struct 2006;1787–817.

[13] Arefi M, Kiani M, Rabczuk T. Application of nonlocal strain gradient theory to size dependent bending analysis of a sandwich porous nanoplate integrated with piezomagnetic face-sheets. Composites B 2019;168:320–33.
[14] Mindlin RD, Eshel N. On first strain-gradient theories in linear elasticity. Int J Solids Struct 1968;4(1):109–24.
[15] Fleck N, Hutchinson J. A phenomenological theory for strain gradient effects in plasticity. J Mech Phys Solids 1993;41(12):1825–57.
[16] Khakalo S, Niiranen J. Form II of mindlin's second strain gradient theory of elasticity with a simplification: For materials and structures from nano-to macro-scales. Eur J Mech A Solids 2018;71:292–319.
[17] Reiher JC, Giorgio I, Bertram A. Finite-element analysis of polyhedra under point and line forces in second-strain gradient elasticity. J Eng Mech 2017;143(2):04016112.
[18] Hadjesfandiari AR, Dargush GF. Couple stress theory for solids. Int J Solids Struct 2011;48(18):2496–510.
[19] Reddy J. Microstructure-dependent couple stress theories of functionally graded beams. J Mech Phys Solids 2011;59(11):2382–99.
[20] Park S, Gao X. Bernoulli–Euler beam model based on a modified couple stress theory. J Micromech Microeng 2006;16(11):2355.
[21] Kahrobaiyan M, Asghari M, Ahmadian M. A Timoshenko beam element based on the modified couple stress theory. Int J Mech Sci 2014;79:75–83.
[22] Eringen A. Simple microfluids. Internat J Engrg Sci 1964;2:205–17.
[23] Eringen A. Linear theory of micropolar elasticity. J Appl Math Mech 1966;15:909–23.
[24] Altenbach H, Naumenko K, Zhilin PA. A micro-polar theory for binary media with application to phase-transitional flow of fiber suspensions. Contin Mech Thermodyn 2003;15:539–70.
[25] Somaiah K, Kumar AR. Rayleigh wave propagation at viscous liquid/micropolar micro-stretch elastic solid. Commun Math Appl 2023;14(1):89.
[26] Vernerey F, Liu WK, Moran B. Multi-scale micromorphic theory for hierarchical materials. J Mech Phys Solids 2007;55(12):2603–51.
[27] Gurtin ME, Murdoch AI. A continuum theory of elastic material surfaces. Arch Ration Mech Anal 1975;57(4):291–323.
[28] Li L, Lin R, Ng TY. Contribution of nonlocality to surface elasticity. Internat J Engrg Sci 2020;152:103311.
[29] Kroner E. Elasticity theory of materials with long range cohesive forces. Int J Solids Struct 1967;3:731–42.
[30] Muc A. Non-local approach to free vibrations and buckling problems for cylindrical nano-structures. Compos Struct 2020;250:112541.
[31] Oates WS. Flexoelectricity, strain gradients, and singularities in ferroelectric nanostructures. J Intell Mater Syst Struct 2017;28(20):3091–105.
[32] Makvandi R, Duczek S, Juhre D. A phase-field fracture model based on strain gradient elasticity. Eng Fract Mech 2019;220:106648.
[33] Mousavi SM, Aifantis EC. Dislocation-based gradient elastic fracture mechanics for in-plane analysis of cracks. Int J Fract 2016;202(1):93–110.
[34] Garg A, Chalak H, Belarbi M, Zenkour A, Sahoo R. Estimation of carbon nanotubes and their applications as reinforcing composite materials–an engineering review. Compos Struct 2021;272:114234.
[35] Ramalingame R, Hu Z, Gerlach C, Rajendran D, Zubkova T, Baumann R, Kanoun O. Flexible piezoresistive sensor matrix based on a carbon nanotube PDMS composite for dynamic pressure distribution measurement. J Sensors Sensor Syst 2019;8(1):1–7.
[36] Esen I, Daikh AA, Eltaher MA. Dynamic response of nonlocal strain gradient FG nanobeam reinforced by carbon nanotubes under moving point load. Eur Phys J Plus 2021;136(4):1–22.
[37] Khorshidi MA. Validation of weakening effect in modified couple stress theory: Dispersion analysis of carbon nanotubes. Int J Mech Sci 2020;170:105358.
[38] Izadi R, Tuna M, Trovalusci P, Ghavanloo E. Torsional characteristics of carbon nanotubes: Micropolar elasticity models and molecular dynamics simulation. Nanomaterials 2021;11:453.
[39] Dindarloo MH, Li L. Vibration analysis of carbon nanotubes reinforced isotropic doubly-curved nanoshells using nonlocal elasticity theory based on a new higher order shear deformation theory. Composites B 2019;175:107170.
[40] Balaji NN, Chen W, Brake MR. Traction-based multi-scale nonlinear dynamic modeling of bolted joints: Formulation, application, and trends in micro-scale interface evolution. Mech Syst Signal Process 2020;139:106615.
[41] Emam SA, Hobeck J, Inman DJ. Experimental investigation into the nonlinear dynamics of a bistable laminate. Nonlinear Dynam 2019;95:3019–39.
[42] Ladurner D, Adam C, Furtmüller T. Geometric nonlinear analysis of slender layered non-prismatic beams with interlayer slip. Int J Mech Sci 2023;108651.
[43] Pietrosanti D, De Angelis M, Giaralis A. Experimental study and numerical modeling of nonlinear dynamic response of SDOF system equipped with tuned mass damper inerter (TMDI) tested on shaking table under harmonic excitation. Int J Mech Sci 2020;184:105762.
[44] Casapulla C, Giresini L, Argiento LU, Maione A. Nonlinear static and dynamic analysis of rocking masonry corners using rigid macro-block modeling. Int J Struct Stab Dyn 2019;19(11):1950137.
[45] Fajfar P, Fischinger M. Mathematical modelling of reinforced concrete structural walls for nonlinear seismic analysis. In: Structural dynamics-Vol 1. Routledge; 2022, p. 471–8.
[46] Vinyas M, Harursampath D. Nonlinear vibrations of magneto-electro-elastic doubly curved shells reinforced with carbon nanotubes. Compos Struct 2020;253:112749.
[47] Strozzi M, Smirnov VV, Manevitch LI, Pellicano F. Nonlinear normal modes, resonances and energy exchange in single-walled carbon nanotubes. Int J Non-Linear Mech 2020;120:103398.
[48] Dat ND, Quan TQ, Mahesh V, Duc ND. Analytical solutions for nonlinear magneto-electro-elastic vibration of smart sandwich plate with carbon nanotube reinforced nanocomposite core in hygrothermal environment. Int J Mech Sci 2020;186:105906.
[49] Ghaffari S, Ceballes S, Abdelkefi A. Nonlinear dynamical responses of forced carbon nanotube-based mass sensors under the influence of thermal loadings. Nonlinear Dynam 2020;100:1013–35.
[50] Rudenko A, Mauclair C, Garrelie F, Stoian R, Colombier J-P. Amplification and regulation of periodic nanostructures in multipulse ultrashort laser-induced surface evolution by electromagnetic-hydrodynamic simulations. Phys Rev B 2019;99(23):235412.
[51] Mastellone M, Bellucci A, Girolami M, Serpente V, Polini R, Orlando S, Santagata A, Sani E, Hitzel F, Trucchi DM. Deep-subwavelength 2D periodic surface nanostructures on diamond by double-pulse femtosecond laser irradiation. Nano Lett 2021;21(10):4477–83.
[52] Lasa-Alonso J, Abujetas DR, Nodar Á, Dionne JA, Sáenz JJ, Molina-Terriza G, Aizpurua J, García-Etxarri A. Surface-enhanced circular dichroism spectroscopy on periodic dual nanostructures. Acs Photonics 2020;7(11):2978–86.
[53] Amalraj TD, Savarimuthu R. Design and analysis of microstrip antenna on periodic and non-periodic photonic band gap substrate. IETE J Res 2022;68(6):4300–9.
[54] Mead D. A general theory of harmonic wave propagation in linear periodic systems with multiple coupling. J Sound Vib 1973;27:235–60.
[55] Furer J, Castañeda PP. Homogenization, macroscopic instabilities and domain formation in magnetoactive composites: Theory and applications. J Mech Phys Solids 2022;169:105081.
[56] Allaire G, Geoffroy-Donders P, Pantz O. Topology optimization of modulated and oriented periodic microstructures by the homogenization method. Comput Math Appl 2019;78(7):2197–229.
[57] Dutra TA, Ferreira RTL, Resende HB, Guimaraes A. Mechanical characterization and asymptotic homogenization of 3D-printed continuous carbon fiber-reinforced thermoplastic. J Braz Soc Mech Sci Eng 2019;41:1–15.
[58] Kalamkarov AL, Hassan EM, Georgiades A, Savi M. Asymptotic homogenization model for 3D grid-reinforced composite structures with generally orthotropic reinforcements. Compos Struct 2009;89(2):186–96.
[59] Christoff BG, Brito-Santana H, Talreja R, Tita V. Multiscale embedded models to determine effective mechanical properties of composite materials: Asymptotic homogenization method combined to finite element method. Compos Part C: Open Access 2022;9:100303.
[60] Wang G, Li S, Nguyen H-N, Sitar N. Effective elastic stiffness for periodic masonry structures via eigenstrain homogenization. J Mater Civ Eng 2007;19(3):269–77.
[61] Garbowski T, Gajewski T. Determination of transverse shear stiffness of sandwich panels with a corrugated core by numerical homogenization. Materials 2021;14(8):1976.
[62] Gupta S, Pramanik S, Das SK, Saha S, et al. Dynamic analysis of wave propagation and buckling phenomena in carbon nanotubes (CNTs). Wave Motion 2021;104:102730.
[63] Asghar S, Naeem MN, Hussain M. Non-local effect on the vibration analysis of double walled carbon nanotubes based on donnell shell theory. Phys E: Low-Dimens Syst Nanostruct 2020;116:113726.
[64] Al-Furjan M, Oyarhossein MA, Habibi M, Safarpour H, Jung DW, Tounsi A. On the wave propagation of the multi-scale hybrid nanocomposite doubly curved viscoelastic panel. Compos Struct 2021;255:112947.
[65] Lazar M, Maugin GA. Nonsingular stress and strain fields of dislocations and disclinations in first strain gradient elasticity. Int J Eng Sci 2005;43(13–14):1157–84.
[66] Lazar M, Maugin GA, Aifantis EC. Dislocations in second strain gradient elasticity. Int J Solids Struct 2006;43(6):1787–817.
[67] Mousavi SM. Dislocation-based fracture mechanics within nonlocal and gradient elasticity of bi-Helmholtz type—Part II: Inplane analysis. Int J Solids Struct 2016;92:105–20.
[68] Abedinnasab MH, Hussein MI. Wave dispersion under finite deformation. Wave Motion 2013;50(3):374–88.
[69] Yang B, Droz C, Zine A, Ichchou M. Dynamic analysis of second strain gradient elasticity through a wave finite element approach. Compos Struct 2021;263:113425.
[70] Mindlin RD. Second gradient of strain and surface tension in linear elasticity. Int J Solids Struct 1965;147–438.
[71] Sakhaee-Pour A. Elastic properties of single-layered graphene sheet. Solid State Commun 2009;149(1–2):91–5.

[72] Scarpa F, Adhikari S. A mechanical equivalence for Poisson's ratio and thickness of C–C bonds in single wall carbon nanotubes. J Phys D: Appl Phys 2008;41(8):085306.
[73] Ramos JI. On Linstedt–Poincaré techniques for the quintic duffing equation. Appl Math Comput 2007;193(2):303–10.
[74] Bunch JS, Van Der Zande AM, Verbridge SS, Frank IW, Tanenbaum DM, Parpia JM, Craighead HG, McEuen PL. Electromechanical resonators from graphene sheets. Science 2007;315(5811):490–3.
[75] Cotoni V, Langley R, Shorter P. A statistical energy analysis subsystem formulation using finite element and periodic structure theory. J Sound Vib 2008;318:1077–108.
[76] Remani C. Numerical methods for solving systems of nonlinear equations, Vol. 77. Ontario, Canada: Lakehead University Thunder Bay; 2013.